Draft version January 12, 2017
Preprint typeset using LaTeX style emulateapj v. 5/2/11

arXiv:1701.03094v1 [astro-ph.SR] 11 Jan 2017

A COMPREHENSIVE OBSERVATIONAL ANALYSIS OF V1324 SCO, THE MOST GAMMA-RAY LUMINOUS CLASSICAL NOVA TO DATE

Thomas Finzell[1], Laura Chomiuk[1], Brian D. Metzger[2], Frederick M. Walter[3], Justin D. Linford[4,5], Koji Mukai[6,7], Thomas Nelson[8], Jennifer H. S. Weston[9], Yong Zheng[2], Jennifer L. Sokoloski[2], Amy Mioduszewski[10], Michael P. Rupen[11], Subo Dong[12], Terry Bohlsen[13], Christian Buil[14], Jose Prieto[15,16], R. Mark Wagner[17,18], Thomas Bensby[19], I..A. Bond[20], T. Sumi[21], D.P. Bennett[22], F. Abe[23], N. Koshimoto[24], D. Suzuki[21], P.,J. Tristram[25], Grant W. Christie[26], Tim Natusch[26], Jennie McCormick[27], Jennifer Yee[28], and Andy Gould[18]

Draft version January 12, 2017

ABSTRACT

It has recently been discovered that some, if not all, classical novae emit GeV gamma-rays during outburst, but the mechanics of this gamma-ray emission are still not well understood. We present here a comprehensive, multi-wavelength dataset—from radio to X-rays—for the most gamma-ray luminous classical nova to-date, V1324 Sco. Using this dataset, we show that V1324 Sco is a canonical dusty Fe-II type nova, with a bulk ejecta velocity of 1150 ± 40 km s^{-1}and an ejecta mass of $2.0 \pm 0.4 \times 10^{-5}$ $M_{\odot}$. However, despite it's seeming normalcy, there is also evidence for complex shock interactions, including the aforementioned gamma-rays and early time high-brightness temperature radio emission. To explain how a nova can be simultaneously ordinary and have the highest gamma-ray luminosity to date we present a simplified model of the ejecta in which the strength of gamma-ray emission is set by properties the fast ejecta component that collides with a slower component to produce shocks. We conclude by detailing how this model can be tested using future gamma-ray detected novae.

Subject headings: novae, cataclysmic variables, AAVSO, gamma rays: stars

[1] Department of Physics and Astronomy, Michigan State Univeristy, 567 Wilson Road, East Lansing, MI 48824-2320
[2] Columbia Astrophysics Laboratory, Columbia University, New York, NY 10027, USA
[3] Department of Physics and Astronomy, Stony Brook University, Stony Brook, NY 11794-3800
[4] Department of Physics, The George Washington University, Washington, DC 20052, USA
[5] Astronomy, Physics, and Statistics Institute of Sciences, The George Washington University, Washington, DC 20052, USA
[6] CRESST and X-ray Astrophysics Laboratory, NASA/GSFC, Greenbelt, MD 20771, USA
[7] Department of Physics, University of Maryland, Baltimore County, 1000 Hilltop Circle, Baltimore, MD 21250, USA
[8] School of Physics and Astronomy, University of Minnesota, 116 Church Street SE, Minneapolis, MN 55455, USA
[9] Green Bank Observatory,P.O. Box 2, Green Bank, WV 24944 USA
[10] National Radio Astronomy Observatory, P.O. Box O, Socorro, NM 87801,USA
[11] National Research Council of Canada, Herzberg Astronomy and Astrophysics Programs, Dominion Radio Astrophysical Observatory
[12] Kavli Institute for Astronomy and Astrophysics, Peking University, Yi He Yuan Road 5, Hai Dian District, Beijing 100871, China
[13] Mirranook Observatory, Boorolong Rd Armidale, NSW, 2350, Australia
[14] Castanet Tolosan Observatory, 6 place Clemence Isaure, 31320 Castanet Tolosan, France
[15] Núcleo de Astronomía de la Facultad de Ingeniería, Universidad Diego Portales, Av. Ejército 441, Santiago, Chile
[16] Millennium Institute of Astrophysics, Santiago, Chile
[17] LBT, University of Arizona, 933 N. Cherry Ave, Room 552, Tucson, AZ 85721, USA
[18] Department of Astronomy, The Ohio State University, Columbus, OH 43210, USA
[19] Lund Observatory, Department of Astronomy and Theoretical Physics, Box 43, SE-221 00 Lund, Sweden
[20] Institute of Information and Mathematical Sciences, Massey University, Private Bag 102-904, North Shore Mail Centre, Auckland, New Zealand
[21] Department of Earth and Space Science, Graduate School of Science, Osaka University, Toyonaka, Osaka 560-0043, Japan
[22] Laboratory for Exoplanets and Stellar Astrophysics, NASA/Goddard Space Flight Center, Greenbelt, MD 20771, USA
[23] Institute for Space-Earth Environmental Research, Nagoya University, Nagoya 464-8601, Japan
[24] Department of Earth and Space Science, Graduate School of Science, Osaka University, Toyonaka, Osaka 560-0043, Japan
[25] Mt. John University Observatory, P.O. Box 56, Lake Tekapo 8770, New Zealand
[26] Auckland Observatory, Auckland, New Zealand
[27] Farm Cove Observatory, Centre for Backyard Astrophysics, Pakuranga, Auckland, New Zealand
[28] Harvard-Smithsonian Center for Astrophysics, 60 Garden Street, Cambridge, MA 02138 USA

1. INTRODUCTION

Classical novae are the result of a thermonuclear runaway taking place on the surface of a white dwarf and are fueled by matter accreted on to the white dwarf from a companion star. These outbursts give rise to an increase in luminosity and eject between $\sim 10^{-3}-10^{-7} M_{\odot}$ of material at velocities $\gtrsim 10^{3}$ km s^{-1} (Gallagher & Starrfield 1978; Prialnik 1986; Yaron et al. 2005; Shore 2012).

Nova outbursts have also been detected in the GeV gamma-ray regime with *Fermi Gamma Ray Space Telescope* (see e.g. Cheung et al. 2010, 2012a,b; Hays et al. 2013; Cheung et al. 2015). The presence of gamma-rays imply that there are relativistic particles being generated in the nova event. There are two potential processes for producing gamma-rays from relativistic particles: the leptonic process and the hadronic process. In the leptonic process electrons are accelerated up to relativistic speeds, and the gamma-rays are produced when photons inverse-Compton scatter off of the non-thermal electrons (Blumenthal & Gould 1970). In the hadronic process, it is ions that are being accelerated to relativistic speeds; these non-thermal protons then collide with a dense medium to produce π^0 mesons, which then decay to gamma-rays (Drury et al. 1994). The likely source of the accelerated particles is strong shocks, which can generate relativistic particles via the diffusive shock acceleration mechanism (Blandford & Ostriker 1978; Metzger et al. 2014). The details of particle acceleration in novae still remains a poorly understood issue, despite the potential for insight into the broader topic of high-energy astrophysics (Metzger et al. 2015).

The first nova detected by *Fermi* was V407 Cyg, and it received considerable attention (Abdo et al. 2010; Aliu et al. 2012; Chomiuk et al. 2012; Esipov et al. 2012; Mukai et al. 2012; Nelson et al. 2012; Orlando & Drake 2012; Shore et al. 2012; Martin & Dubus 2013). Given that V407 Cyg has a Mira giant secondary with a dense wind (a member of the symbiotic class of systems), a model to explain the gamma-rays was proposed wherein a shock was generated as the nova ejecta interacted with the dense ambient medium.

This model, however, failed to explain subsequent novae detected by *Fermi*: V1324 Sco, V959 Mon, V339 Del (Ackermann et al. 2014), V1369 Cen (Cheung et al. 2013), and V5668 Sgr (Cheung et al. 2015), almost all of which do not have a detectable red-giant companion (see, e.g., Finzell et al. 2015; Munari et al. 2013; Munari & Henden 2013; Hornoch 2013; the progenitor of V5589 Sgr has yet to be determined). While it is theoretically possible for these novae to have high density circumstellar material despite not having a red-giant companion (Spruit & Taam 2001), no evidence has yet been found for dusty circumstellar material around cataclysmic variables (Harrison et al. 2013). Thus the fact that red-giant companions were not detected implies that these novae have main-sequence companions with low-density circumstellar material.

It is in fact much more likely that the shocks are being produced within the ejecta, due to different components of the ejecta colliding with one another (internal shocks). There has already been long standing evidence for internal shocks in classical novae from X-ray observations (Mukai & Ishida 2001). However, some asymmetry in the mass ejection mechanism is necessary in order to generate internal shocks. One idea put forward by Chomiuk et al. (2014) is that there is a common envelope phase during the mass ejection, resulting in a density enhancement in the binary orbital plane. A separate, fast, and diffuse wind propagates in the polar direction (e.g. perpendicular to the orbital plane). When these two outflows—dense equatorial and diffuse polar—collide with one another, they produce shocks.

Progress has been made on the theoretical front, by constraining the conditions necessary for both the thermal emission (Metzger et al. 2014) and non-thermal emission (Vlasov et al. 2016) observed in gamma-ray detected novae. Work done in Metzger et al. (2015) found that a significant fraction ($> 10\%$) of the bolometric light should be coming from shock emission. However, there has been little in the way of in-depth, multi-wavelength, analysis of these gamma-ray novae on the observational side, to constrain the properties of the shock.

It is critical that a multi-wavelength analysis is used, as each of the different spectral regimes provides a different piece of the puzzle. From the X-rays we can constrain the shock environment (e.g., Mukai & Ishida 2001; Mukai et al. 2008); from the optical and IR we gain information about the energetics and structure of the ejecta (e.g. Hutchings 1972; Hachisu & Kato 2016); from the radio, we can determine bulk ejecta properties such as mass and velocity (e.g. Seaquist & Palimaka 1977; Hjellming et al. 1979). Finally, we must also construct a model that can produce non-thermal particle acceleration, to facilitate gamma-ray production. It is only possible to disentangle the complexity of nova events by leveraging the information gained from each wavelength regime. Here we present the first such multi-wavelength analysis of the most gamma-ray luminous nova, V1324 Sco.

We present the results from our analysis of V1324 Sco using data from the optical/near-IR, radio, and X-ray (limits). This paper begins by presenting the complete multi-wavelength dataset we have gathered for V1324 Sco: in Section 2 we discuss the optical/near-IR photometry; in Section 3 we discuss the optical spectra; in Section 4 we detail the X-ray limits; and in Section 5 we discuss our radio data. In Section 6 we show that V1324 Sco is—in all non-gamma-ray observations—a normal nova; we discuss how a normal nova can also be the most luminous gamma-ray nova observed to date; we present a model that explains this seemingly paradoxical situation; and we also present a means of testing said model. Finally, we conclude the paper in Section 7 by summarizing our findings for V1324 Sco and lessons learned for future observations of gamma-ray novae.

2. OPTICAL/NEAR-IR PHOTOMETRY

2.1. *Observations and Reduction*

V1324 Sco falls within one of the fields that the Microlensing Observations in Astrophysics (MOA) Collaboration continually observe with the MOAII 1.8 meter telescope at Mt. Johns Observatory in New Zealand. V1324 Sco was initially detected in 2012 May by their high-cadence I-band photometry (Wagner et al. 2012). The initial detection showed a slow monotonic rise in brightness between May 14 - May 31 (see Figure 1), followed by a very large increase in brightness starting June

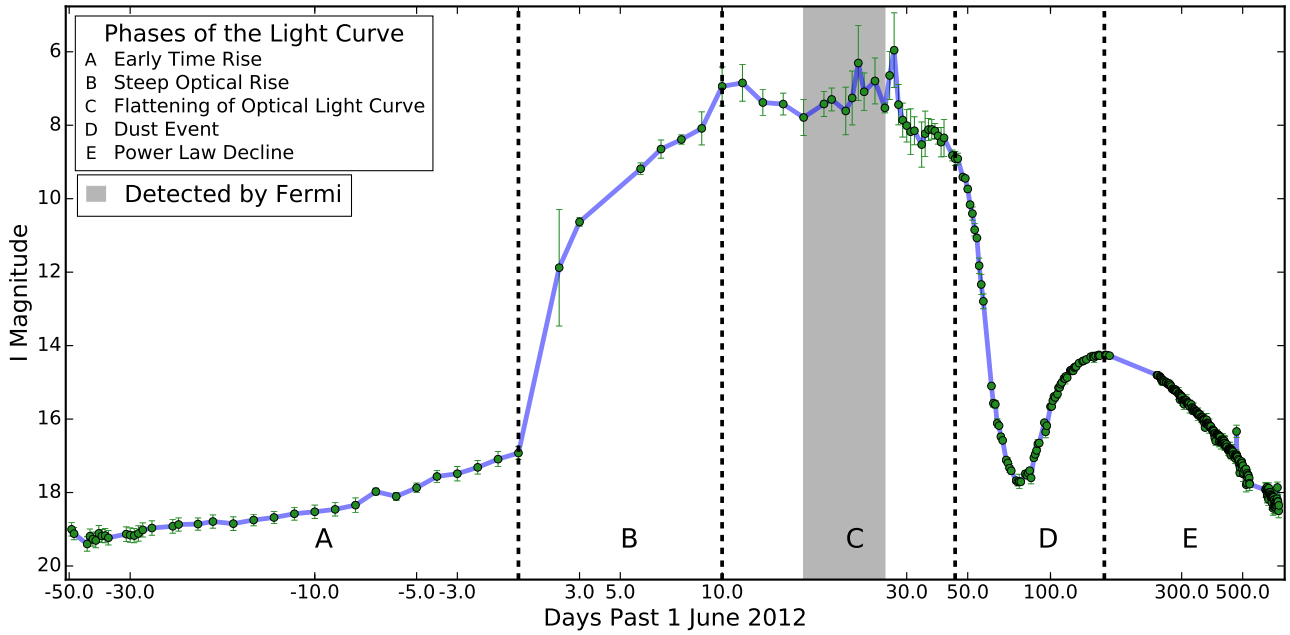

Figure 1. I band light curve for V1324 Sco, generated using the MOA data set. The plot starts 49 days before primary optical rise, at the first date where a *single* observation (as opposed to a stacked observation) yields a 5σ detection. The gray shaded region denotes the time period where V1324 Sco was detected in gamma-rays. Thanks to the extremely high time-resolution of the MOA data set we can see all of the different evolutionary phases of the optical light curve, as discussed in section 2.2. Note that the X-axis takes the date of the primary optical rise (1 June 2012) to be day 0, so the plot starts on a negative value.

1 (Wagner et al. 2012). We will take June 1 to be day 0. We also adopt the convention throughout this paper that all dates with − or + denote days before or after 1 June 2012, respectively.

All initial high-cadence observations, taken as part of the regular MOA program, were taken in the I-broad band, and were reduced using the standard procedure (see Bond et al. 2001 for details). The MOA survey emphasizes rapid imaging of the Galactic bulge fields; on a clear night an individual field will be reimaged every $\sim$ 40 minutes. The result of this high time cadence photometry can be seen in Figure 1. It should be noted that the primary purpose of the high-cadence observations is difference imaging; as a result, the individual values should only be used to measure changes, not as an absolute measurement (Bond et al. 2001).

After the steep optical rise a follow up campaign was triggered by the MicroFUN group[29], who believed that the transient was a potential microlensing event. Apart from the standard I-broad band filter, the MicroFUN follow up observations also used V and I Bessel filters. Other observations were made in B, V, and I filters using the Small & Moderate Aperture Research Telescope System (SMARTS) 1.3 Meter telescope and Auckland Observatories.

Along with the MOA and MicroFUN data we also present multi-color photometry from Fred Walter's ongoing Stony Brook/SMARTS Atlas of (mostly) Southern Novae (see Walter et al. 2012 for further information on this dataset), as well as data from American Association of Variable Star Observers (AAVSO)[30]. The SMARTS data uses the ANDICAM instrument on the 1.3 meter telescope, and provide both optical (B, V, R, I) and near-IR (J, H, K) filters going from day +35 to day +124, while the AAVSO data have optical (V, B, R) filters, and goes from day +7 to day +445. A portion of the optical photometric data set is presented in Table 1; the entire data set can be found in the online publication. Note that no attempt has been made to standardize the photometry from different observatories.

[29] http://www.astronomy.ohio-state.edu/~microfun/
[30] https://www.aavso.org/data-download

2.2. *Timeline of Optical Light curve*

We give an overview of the different phases in the evolution of the optical light curve, to help orient the reader to the different qualitative variations. Throughout this overview we will reference Figure 1, which shows the light curve generated from the MOA data set. We will also reference Figure 2—which shows the light curve for multiple photometric bands as well as the color evolution—whenever there is multi-band photometry for a given evolutionary phase.

2.2.1. *Early Time Rise (Days −49 to 0)*

The first MOA observation of V1324 Sco that was a 5σ detection occurred on 13 April 2012. Following this there was a monotonic increase in brightness that lasted until 31 May 2012. The total increase in brightness during this period was $\Delta I \approx 2.5$ mags (about ~ 0.05 mags per day). This can be seen as phase A of Figure 1. An analysis of this initial rise can be found in Wagner et al. (In prep).

This type of behavior has never been observed in novae before, although this could be a selection effect. Most early time information for novae comes from the Solar Mass Ejection Imager (SMEI) (Hounsell et al. 2010), which has a limiting magnitude of $m_{\rm SMEI} \sim 8$, preventing it from seeing such faint early time rises. It is only with the type of dedicated, deep, high cadence observations

Table 1
Table of Photometric Data

Observation Date	JD	$t - t_0$[a] (Days)	Filter	Mag	Mag Error	Observer/Group	Telescope/Specific Filter[b]
2012 Apr 13	2456030.07502	-48.92499	I	18.700	0.150	MOA	MJUO-Ibroad
2012 Apr 13	2456030.95591	-48.04410	I	18.770	0.090	MOA	MJUO-Ibroad
2012 Apr 13	2456030.95714	-48.04287	I	18.590	0.090	MOA	MJUO-Ibroad
2012 Apr 13	2456030.99663	-48.00338	I	18.800	0.110	MOA	MJUO-Ibroad
2012 Apr 14	2456031.05194	-47.94807	I	18.760	0.090	MOA	MJUO-Ibroad
2012 Apr 14	2456031.06304	-47.93697	I	18.900	0.110	MOA	MJUO-Ibroad
2012 Apr 14	2456031.07414	-47.92587	I	18.850	0.090	MOA	MJUO-Ibroad
2012 Apr 14	2456031.08652	-47.91348	I	18.860	0.110	MOA	MJUO-Ibroad
2012 Apr 14	2456031.09762	-47.90238	I	19.030	0.110	MOA	MJUO-Ibroad
2012 Apr 14	2456031.10976	-47.89024	I	18.660	0.070	MOA	MJUO-Ibroad
2012 Apr 14	2456031.12211	-47.87789	I	18.930	0.120	MOA	MJUO-Ibroad
2012 Apr 14	2456031.13321	-47.86679	I	18.890	0.100	MOA	MJUO-Ibroad
2012 Apr 14	2456031.14435	-47.85566	I	18.830	0.100	MOA	MJUO-Ibroad
2012 Apr 14	2456031.15670	-47.84331	I	18.860	0.090	MOA	MJUO-Ibroad
2012 Apr 14	2456031.16781	-47.83220	I	18.950	0.110	MOA	MJUO-Ibroad
2012 Apr 14	2456031.17893	-47.82108	I	18.890	0.090	MOA	MJUO-Ibroad
2012 Apr 14	2456031.19127	-47.80874	I	18.910	0.090	MOA	MJUO-Ibroad
2012 Apr 14	2456031.20237	-47.79764	I	18.880	0.120	MOA	MJUO-Ibroad
2012 Apr 14	2456031.21348	-47.78653	I	18.850	0.090	MOA	MJUO-Ibroad
2012 Apr 14	2456031.22585	-47.77416	I	18.880	0.100	MOA	MJUO-Ibroad
2012 Apr 14	2456031.23825	-47.76176	I	18.750	0.090	MOA	MJUO-Ibroad
2012 Apr 14	2456031.25182	-47.74818	I	18.870	0.090	MOA	MJUO-Ibroad
2012 Apr 14	2456031.96000	-47.04001	I	18.610	0.080	MOA	MJUO-Ibroad
2012 Apr 14	2456031.96123	-47.03877	I	18.700	0.080	MOA	MJUO-Ibroad
2012 Apr 14	2456031.99908	-47.00093	I	18.880	0.120	MOA	MJUO-Ibroad
2012 Apr 15	2456032.05184	-46.94817	I	18.740	0.100	MOA	MJUO-Ibroad
2012 Apr 15	2456032.07405	-46.92596	I	18.840	0.130	MOA	MJUO-Ibroad
2012 Apr 15	2456032.08742	-46.91258	I	18.920	0.100	MOA	MJUO-Ibroad
2012 Apr 15	2456032.09855	-46.90146	I	18.810	0.100	MOA	MJUO-Ibroad
2012 Apr 15	2456032.10966	-46.89035	I	18.770	0.090	MOA	MJUO-Ibroad
2012 Apr 15	2456032.12200	-46.87801	I	18.880	0.150	MOA	MJUO-Ibroad
2012 Apr 15	2456032.13311	-46.86690	I	18.740	0.100	MOA	MJUO-Ibroad
2012 Apr 15	2456032.14421	-46.85580	I	18.850	0.100	MOA	MJUO-Ibroad
2012 Apr 15	2456032.15655	-46.84346	I	18.740	0.090	MOA	MJUO-Ibroad
2012 Apr 15	2456032.16869	-46.83132	I	18.780	0.090	MOA	MJUO-Ibroad
2012 Apr 15	2456032.17989	-46.82012	I	18.910	0.090	MOA	MJUO-Ibroad
2012 Apr 15	2456032.19224	-46.80777	I	18.960	0.100	MOA	MJUO-Ibroad
2012 Apr 15	2456032.20335	-46.79666	I	18.890	0.080	MOA	MJUO-Ibroad
2012 Apr 15	2456032.21445	-46.78556	I	18.800	0.080	MOA	MJUO-Ibroad
2012 Apr 15	2456032.22683	-46.77317	I	18.840	0.070	MOA	MJUO-Ibroad
2012 Apr 15	2456032.23920	-46.76081	I	18.840	0.100	MOA	MJUO-Ibroad
2012 Apr 15	2456032.25030	-46.74971	I	18.820	0.080	MOA	MJUO-Ibroad
2012 Apr 15	2456032.26264	-46.73736	I	18.960	0.190	MOA	MJUO-Ibroad
...	...	...	...	...	...	...	...

Note. — All of this data, as well data from both AAVSO and (Walter et al. 2012), can be found online.

[a] Taking t_0 to be 1.0 June 2012

[b] This is a key for the different facilities used by the MOA and MicroFUN groups. **MJUO**: Mt. John University Observatory; **AUCK**: Auckland Observatory; **CTIO**: SMARTS 1.3 Meter Telescope.

like those of MOA that we can observe such a rise—although it may be possible in the future with deep surveys like LSST (LSST Science Collaboration et al. 2009).

2.2.2. *Onset of Steep Optical Rise (Days 0 to +10)*

The slow monotonic rise is followed by an extremely rapid increase in brightness; between day 0 and day +2 the brightness increased by ~ 2.2 mags day^{-1}. However, this is just an average, as no measurements were taken on day +1. Between days +2.8 and +3.3 the rate of increase in brightness had dropped to ≈ 1.1 mags day^{-1}, and then between days +5.6 and +6.8 the rate had dropped again, down to ≈ 0.3 mags day^{-1}. This rate of increase persisted for the next two observation epochs (days +7.6 to +7.9 and +8.7 to +9.2), before becoming flat (i.e. ~ 0 mags day^{-1}) starting at the next observation epoch (days +12.9 to +13.2). During this time period (day 0 to +12.9) the I band flux increased by a total of ≈ 9.1 magnitudes, with most of that coming from the first ≈ 3 days. This can be seen as phase B of Figure 1.

2.2.3. *Flattening of the Optical Light Curve (Days +11 to +45)*

The enormous increase in the optical is followed by a period with a much smaller change in brightness, with I changing by ≤ 1.5 mags over the course of the next ~ 30 days. This types of flattening in the light curve are not unique to V1324 Sco; Strope et al. (2010) has ~ 15 that show a similar flattening around peak, ~ 10 of which also show a dust event. This can be seen as phase C of Figure 1.

It is during the flattening of the optical light curve that we see both the gamma-ray emission as well as the beginning of the initial radio bump (see section 6 for further details). It should be noted that, of the gamma-

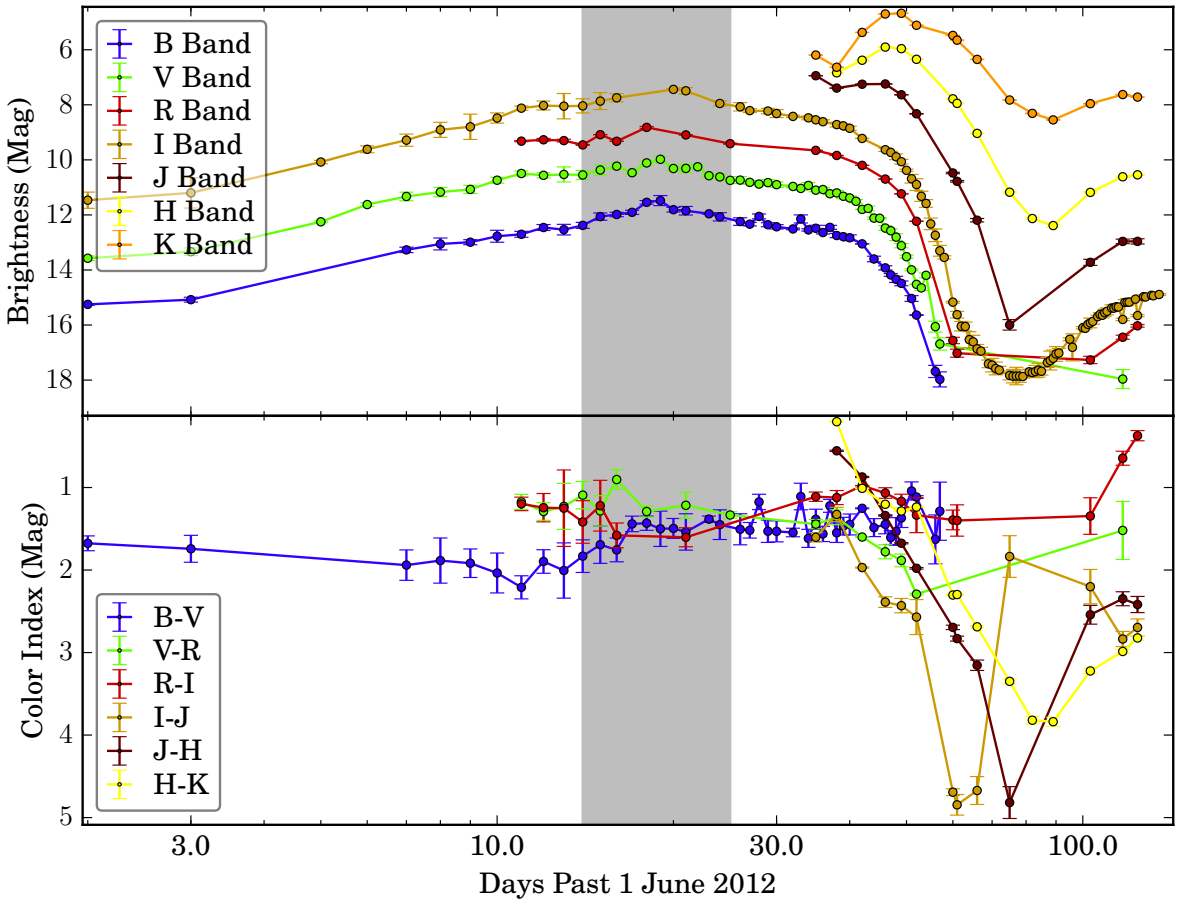

Figure 2. Top panel: Light curves of V1324 Sco in the optical/near-IR bands. Bottom panel: Evolution of optical and near-IR colors. The gray shaded region denotes the time period when V1324 Sco was detected in gamma-rays. Note that this plot has significantly worse time resolution than in Figure 1. Using this figure we can see how the dust event hits the bluer bands first and then moves to redder wavelengths as time progresses. We can also see that the dust event caused a drop in brightness all the way out to the near-IR (JHK) wavelength regime.

ray detected novae, at least two—V1369 Cen and V5668 Sgr—had similar flattening of the optical light curve near maximum (Cheung et al. 2016), though both had a large ($\Delta V > 1$ Mag) oscillations during their period of flattening.

2.2.4. *Dust Event (Days +46 to +157)*

The flattening of the optical light curve is followed by another rapid change in brightness, this time downwards. There was a very clear, very large, decline in optical and near-IR flux that took place from day +46 to day +78, and a subsequent recovery from day +79 to day +157. Only the MOA I band data had the cadence necessary to capture the minimum of the decrease; the I-band flux dropped by ~ 8.5 magnitudes in the span of ~ 30 days (Phase D in Figure 1). The observations in BVR did not have the sensitivity to detect V1324 Sco at the bottom of the decline. Figure 2 shows that this decline in flux occurred all the way out to the near-IR (although the decrease is much less in the near-IR bands, i.e. only ~ 3.9 mags in K band). This decline in flux that preferentially affects the shorter wavelength (bluer) light is the signature of a dust event.

A dust event occurs in a nova when the ejecta achieve conditions that are conducive to the condensation of dust—e.g. colder and shielded from ionizing radiation (Gallagher 1977). The newly formed dust has a large optical depth; as a result a new, cooler, photosphere is created at the site of dust condensation. Dust events in novae are not a new phenomenon; McLaughlin (1936) first proposed dust condensation to explain the significant decline in optical light seen in DQ Her.

The standard model of novae posits that the total luminosity of the ejecta remains constant, being powered by the luminosity of the still hot white dwarf at the center of the ejecta (Gallagher & Code 1974; Bath & Shaviv 1976), such that the fraction of the luminosity that is lost in the blue is compensated by increased luminosity in the red. This is only feasible if the cool dusty photosphere is significantly larger than the pre-dust photosphere (Gehrz et al. 1992). However, the details of this larger dust photosphere remain poorly understood. For a blackbody of constant luminosity $R^2 \propto T_{\rm eff}^4 \rightarrow R \propto T_{\rm eff}^2$, so even modest changes in temperature require a significant increase

Table 2
Optical Spectroscopic Observations

UT Date	$t - t_0$ (Days)	Observer	Telescope	Instrument	Dispersion (Å)	Wavelength Range (Å)
2012 Jun 04.0	+3	Bensby	VLT	UVES	0.02	3700 – 9500
2012 Jun 08.5	+7	Bohlsen	Vixen VC200L	LISA	0.5	3800 – 8000
2012 Jun 14.5	+13	Bohlsen	Vixen VC200L	LISA	0.5	3800 – 8000
2012 Jun 18.5	+17	Bohlsen	Vixen VC200L	LISA	0.5	3800 – 8000
2012 Jun 20.9	+19	Buil	0.28 meter Celestron	LISA	~ 0.6	3700 – 7250
2012 Jun 21.2	+20	Walter	SMARTS 1.5m	RC	~ 5.5	3240 – 9500
2012 Jun 23.1	+22	Walter	SMARTS 1.5m	RC	~ 1.0	5620 – 6940
2012 Jun 24.9	+24	Buil	0.28 meter Celestron	LISA	6.2	3700 – 7250
2012 Jun 25.1	+24	Walter	SMARTS 1.5m	RC	~ 1.5	3650 – 5420
2012 Jul 03.0	+32	Walter	SMARTS 1.5m	RC	~ 1.5	3650 – 5420
2012 Jul 07.1	+36	Walter	SMARTS 1.5m	RC	~ 1.0	5620 – 6940
2012 Jul 11.1	+40	Walter	SMARTS 1.5m	RC	~ 5.5	3240 – 9500
2012 Jul 15.0	+44	Walter	SMARTS 1.5m	RC	~ 1.0	5620 – 6940
2012 Jul 16.1	+45	Chomiuk	Clay Magellan	MIKE	0.035	3700 – 9200
2012 Jul 19.0	+48	Walter	SMARTS 1.5m	RC	~ 5.5	3240 – 9500
2013 May 20.0	+353	Wagner	LBT	MODS1	~ 0.5	3420 – 10000
2013 Aug 04.0	+450	Chomiuk	SOAR	Goodman	~ 1.0	3000 – 7000

in photosphere size.

In the case of V1324 Sco, the drop in flux all the way out to the near-IR suggests that the dust photosphere was very cold, and the change in temperature was significant. A rough calculation using the near-IR colors at the epoch closest to the I band minimum suggest that the dust photosphere was < 1000 K. While these types of dust episodes are not unheard of— Strope et al. (2010) gives 16 examples of other such novae—there are only a few novae with dust dips showing comparably cool photospheres (e.g. QV Vul and V1280 Sco; Gehrz et al. 1992; Sakon et al. 2015). For a more thorough analysis of the dust event in V1324 Sco see Derdzinski et al. (2016).

2.2.5. *Power Law Decline (Days +157 to End of Monitoring)*

Following the post-dust event rebound the evolution followed a power law decline, with $I \propto (t - t_0)^{0.2}$ (where t_0 is 1 June 2012). The index of the power law is positive because luminosity *decreases* when magnitudes *increase*. This decline continues until the final observation form April 2014, when it fell below the MOA detection threshold. In terms of Figure 1, the power-law decline is phase E, between day +228 and +730.

3. OPTICAL SPECTRA

3.1. *Observations and Reduction*

We present the spectral observations in a manner similar to the work of Surina et al. (2014)—who carried out a multi-wavelength analysis of the 2011 outburst of T Pyx—by breaking up the analysis into sections based on the phases of the light curve. However, unlike Surina et al. (2014)—where the time frame is relative to the date of V band maximum—all dates presented in this work are relative to the onset of the steep optical rise (taken to be 1 June 2012). All spectroscopic observations—including date, telescope, and observer—are listed in Table 2. Note that all plots have been corrected to put them into the *local standard of rest* velocity frame, not the heliocentric frame.

The details of the data reduction for the UVES and MIKE data can be found in Finzell et al. (2015) and Walter et al. (2012) for the RC Spectrograph data. The SOAR Goodman data were taken using 400 l/mm grating centered at 5000 Å, and were reduced using the standard procedure in IRAF with optimal extraction and wavelength calibration using FeAr arcs. In the case of the spectra taken by C. Buil and T. Bohlsen, both observers used a LISA spectrograph attached to commercially available telescopes of different sizes (0.28 meter Celestron for Buil; 0.22 meter Vixen VC200L for Bohlsen). More information about their observations can be found on their websites[31,32].

3.2. *Spectroscopic Evolution*

3.2.1. *Onset of Steep Optical Rise (Days +4 to +7)*

V1324 Sco presented initially as a standard Fe II type nova. As seen in Figure 3 there were strong P-Cygni absorption profiles starting at least as early as day +3. The Hα emission component peaked at ~ -180 km s^{-1} on day +3, and had a Gaussian FWHM of ~ 800 km s^{-1}. The Hα P-Cygni absorption component had a FWHM of ~ 200 km s^{-1}. The entirety of the Hα, including both the primary emission feature as well as the P-Cygni absorption, extends out to ~ -1100 km s^{-1} in the blue, or ~ 900 km s^{-1} away from line peak. We take the P-Cygni absorption profile to be coming from the fastest material, meaning that—at this early time—the expansion velocity was ~ 900 km s^{-1}.

As discussed in Schwarz et al. (2001), one would normally expect the bulk of the ejecta to be optically thick at these early times and, as a result, one would expect the spectral features to be absorption dominated. The presence of emission in the spectral features—which necessitates an optically thin region in the ejecta—suggests that the nova atmosphere is highly extended, even at this early stage.

The second most prominent features—aside from the Balmer lines—are the Fe II lines, all of which showed P-Cygni profiles. This is evident in Figures 4 and 5, which show the time evolution of the blue (3900 – 4950 Å) and red (5700 – 6400 Å) spectral regions, respectively. In the UVES spectrum taken on day +3 there were Fe II

[31] http://users.northnet.com.au/~bohlsen/Nova/
[32] http://www.astrosurf.com/buil/index.htm

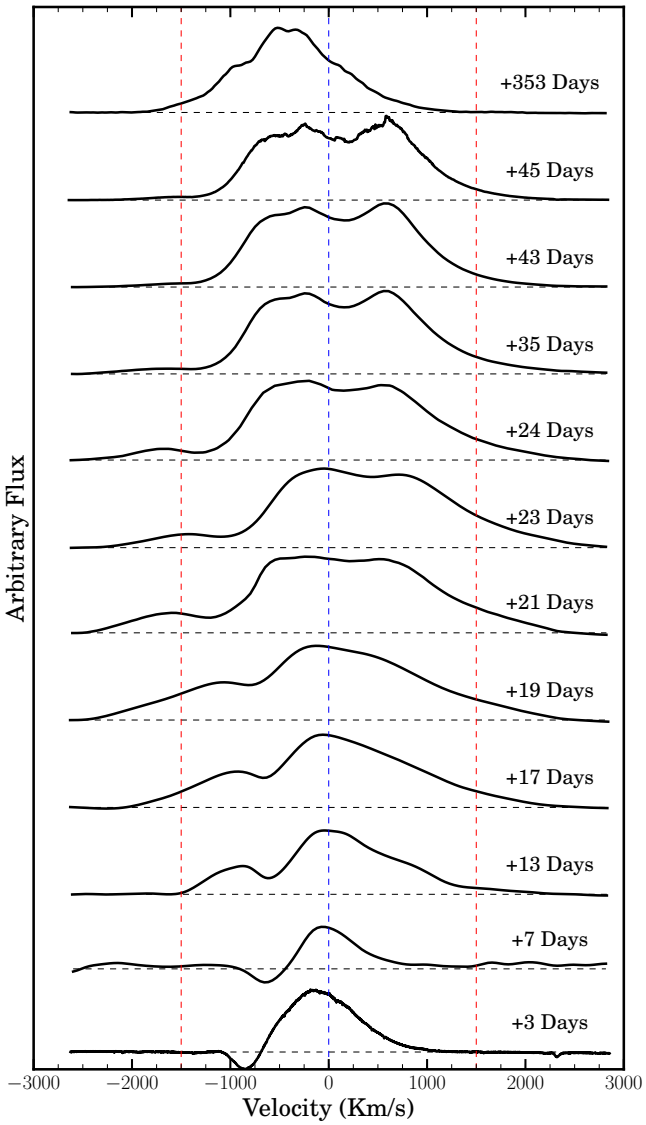

Figure 3. Evolution of the Hα line as a function of time. We take day 0 to be June 1 2012. All velocities are given in terms of the local standard of rest. The blue dashed line indicates $v = 0$ km s^{-1}, while the red dashed lines—used to help guide the eye—give $v = \pm 1500$ km s^{-1}. The $y-$axis is some arbitrary flux; these relative flux values are not to scale. Note the expansion of the velocity profile starting sometime between day +7 and +13, and continuing until day $\sim$ +35.

lines at 4297 Å, 4556 Å, 4584 Å, 4629 Å, 4921 Å, and 6456 Å. There are further lines in the region between 4450 - 4540 angstroms; however, their morphology and velocity structure make them difficult to identify. There is also a feature that could not be identified using the table provided in Williams (2012) that shows a P-Cygni profile and peaks around 4485 Å. It is possible that this is a blend of the Mg II feature at 4481 Å and Fe II feature at 4491 Å.

During this early time we see transitory Si II absorption features at 3858 Å, 5958/78 Å and 6347/71 Å. While present on day +3 all evidence of them disappears by day +22, when the next medium-resolution spectrum was taken. These are the highest excitation lines we see at this early time—having an ionization potential of 16.3 eV—so we attribute the appearance of these absorption features as being evidence of a slightly harder ionizing radiation field at early times, as compared to late times (Hillman et al. 2014).

3.2.2. *Flattening of the Optical Light Curve (Days +13 to +45)*

This period is demarcated by two qualitative changes: an increase in the Hα linewidth (see Figure 3), as well as the onset of the optical decline (i.e. post-maximum stage). This type of increase in the linewidths has been seen before (for some more recent examples see, e.g. Schwarz et al. 2001; Surina et al. 2014). In previous works this increase in linewidth was attributed to a gradually accelerating radiatively driven wind. We discuss this further in Section 6.2.1.

3.2.3. *Nebular Phase*

Within just a few days of the Magellan MIKE spectrum—taken on day +45—V1324 Sco underwent a massive dust dip, dropping by > 8 mags in I band in ~ 30 days, ultimately bottoming out at $I \simeq 17.7$. It was at $I > 16.0$ magnitude for the next ~ 50 days. Although it did eventually rebound out of the dust dip, there was only a brief window of $\sim<$ 25 days before it went into solar conjunction. As a result our spectroscopic coverage did not pick back up until 20 May 2013—355 days after eruption—well into the nebular phase. All of our analysis and line identification is done using the LBT spectrum taken on day +355, as it had better resolution and significantly better S/N.

As seen in Figure 7 the strongest lines in the nebular phase are the [O III] lines at 5007 and 4959 Å, followed by Hα and [Fe VII] at 6084 Å. A list of all of the observed nebular lines is given in Table 3. Most of the lines were matched using the table provided in the appendix of Williams (2012)

There are several lines that seem to have a match but, assuming they are matched correctly, have a peak velocity that is significantly different than the other lines. Such lines include He II at 8237 Å, which would have a peak velocity of $\sim$ 0 km s^{-1}, C I at 8335 Å, which would have a peak velocity of +100 km s^{-1}, and [S III] at 9531 Å, which would also have a peak velocity of +100 km s^{-1} . This is in contrast to most of the other lines, which have peak velocities between -200 to -350 km s^{-1}.

4. X-RAY

Multiple X-ray observations were made using the *Swift* X-Ray Telescope (XRT), all of them yielding non-detections. That is, we did not detect thermal X-rays from the shocked plasma, and we did not detect non-thermal (hard) X-rays from the population of accelerated particles. This is especially noteworthy given that the extremely high gamma-ray luminosity should imply a relatively strong shock which, in turn, would generate a significant amount of hard X-rays (Mukai & Ishida 2001). As discussed in Vurm & Metzger (2016), this apparent contradiction can be explained by either the presence of high densities behind the radiative shock—due to coulomb collisions sapping energy from what would otherwise be X-ray emitting particles—or by bound-free

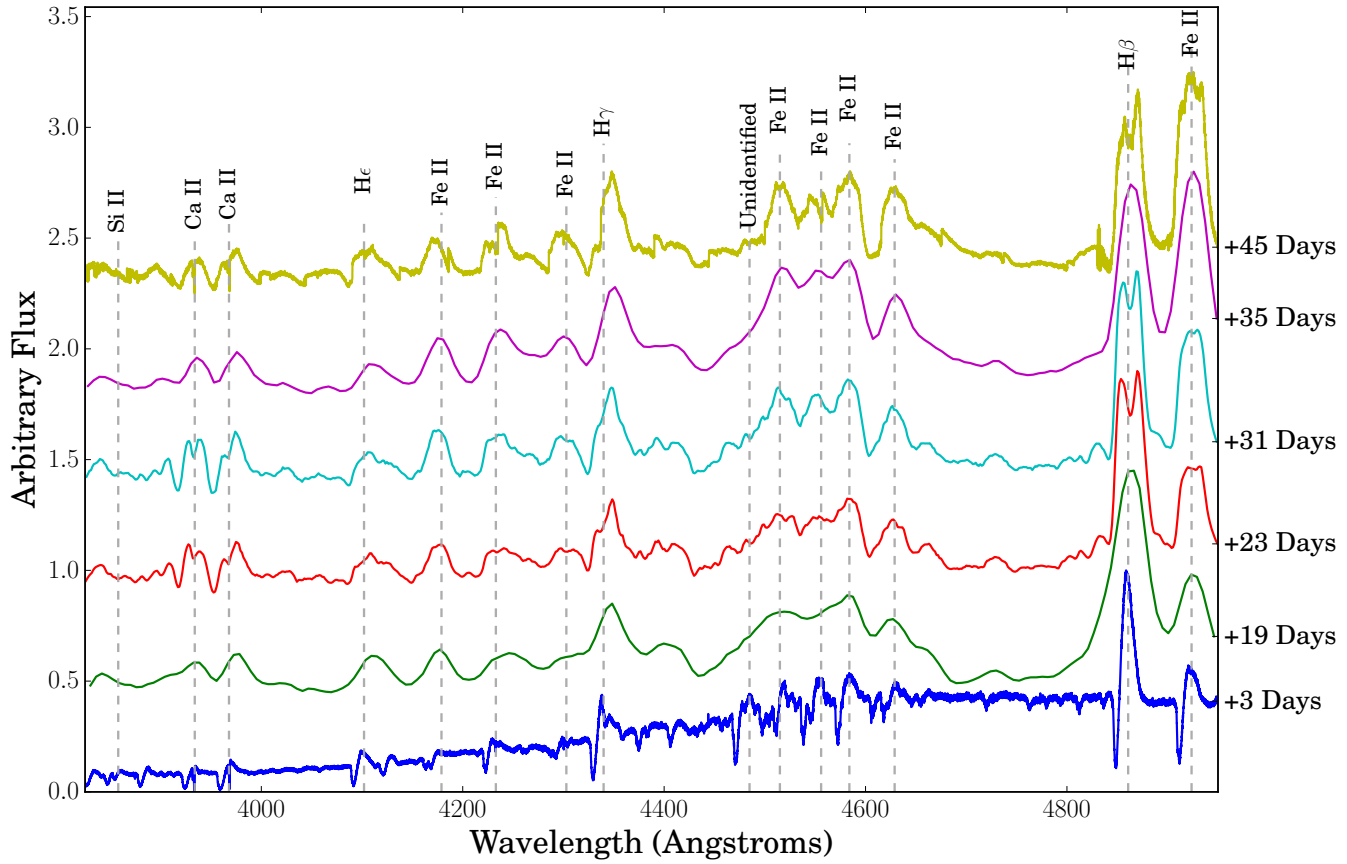

Figure 4. Evolution of the blue ($3900 - 4950$ Å) spectral region. All wavelengths have been corrected to be in the local standard of rest frame. None of these spectra have been corrected for Telluric features.

Table 3
Nebular Phase Spectral Lines

Feature	Wavelength (Å)	Peak Velocity ((km s^{-1}))
[O III]	4363	-140 ± 120
N II	4638	0 ± 100
He II	4686	-200 ± 100
Hβ	4861	-130 ± 170
[O III]	4959	-150 ± 100
[O III]	5007	-160 ± 90
[Fe VII]	5176	-250 ± 100
[Fe VI]	5424	-200 ± 200 (low S/N)
[Fe VII]	5721	-200 ± 100
[N II]	5755	-250 ± 100
[Fe VII]	6084	-280 ± 120
[Ar V]	7006	-250 ± 100
Hα	6563	-400 ± 100
[Ar V]	7006	-250 ± 100
[Ca II]	7057	-80 ± 40
[Ar III]	7136	-250 ± 100
[Ar IV]	7237	-250 ± 100
[O II]	7320/7330	?? (Lines blended)
[S I]	7725	-350 ± 20
He II	8237	$+100 \pm 20$
C I	8335	0 ± 50
[S III]	9069	0 ± 80
[S III]	9531	$+100 \pm 20$

(photoelectric) absorption or inelastic Compton downscattering if there is a large column of material ($\gtrsim 10^{25}$ cm^{-2}) ahead of the shock. In Appendix B we use oxygen line ratios to show such high column densities are plausible.

Note that, along with the peculiar lack of hard X-rays from non-thermal particle acceleration, there was also a lack of soft X-rays, which are usually seen at later times (see, e.g., Schwarz et al. 2011). However, V1324 Sco was both distant ($\geq$ 6.5 kpc Finzell et al. 2015) and had a large absorbing column density. The only other nova given in Schwarz et al. (2011) with both of these characteristics is V1663 Aql, a nova that was also never detected as a super soft source.

We present the X-ray limits obtained from the *Swift* observations in Table 4. The quoted limits are the 3σ upper limits, derived using the Bayesian upper limit method outlined in Kraft et al. (1991). The count rates were converted into luminosities assuming emission from a thermal plasma with characteristic temperature 1 keV and a distance of 6.5 kpc(which is lower limit derived in Finzell et al. 2015). These limits are for X-ray luminosities in the range $0.3 - 10$ keV. The luminosity limits only correct for absorption by the ISM, assuming a column density of 8×10^{21} cm^{-2}. The column density was derived using the reddening values of Finzell et al. (2015) and the relationship of Güver & Oumlzel (2009). These limits were used in the analysis of Metzger et al. (2014) and we are publishing the actual numbers here for completeness.

5. RADIO DATA

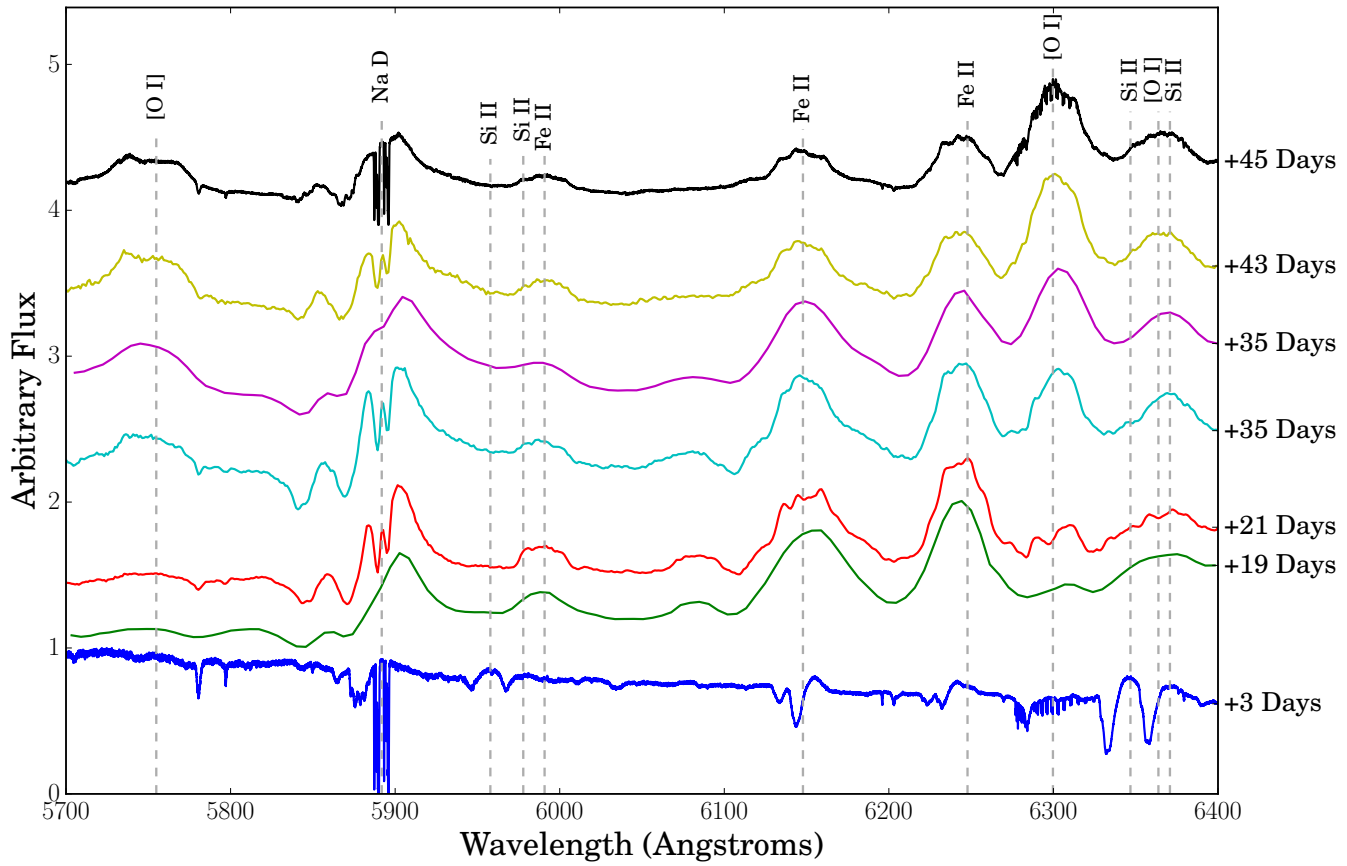

Figure 5. Evolution of the red (5700 − 6400 Å) spectral region. All wavelengths have been corrected to be in the local standard of rest frame. None of these spectra have been corrected for Telluric features. The UVES spectrum taken on day +3 has contamination from Telluric absorption lines between 6280 Å and 6320 Å .

Table 4
X-ray Upper Limits from *Swift* XRT

Date (UT)	$t - t_0$ (Days)	Count Rate[a] (s^{-1})	Luminosity[a] (ergs s^{-1} cm^{-2})
2012 Jun 22	+21	0.0031	1.66465E+33
2012 Jun 27	+26	0.0054	2.9068E+33
2012 Jun 28	+27	0.0151	8.112E+33
2012 Jul 4	+33	0.0038	2.0449E+33
2012 Jul 10	+39	0.012	6.4389E+33
2012 Jul 13	+42	0.0055	2.9575E+33
2012 Aug 14	+74	0.0031	1.66465E+33
2012 Oct 16	+137	0.0023	1.23539E+33
2013 May 22	+355	0.003	1.61226E+33
2013 Nov 3	+520	0.0037	1.9942E+33

[a] 3σ Upper limits

Radio emission from novae is a crucial tool in our analysis, as the opacity at radio frequencies is directly proportional to the emission measure—defined for some line of sight z as $EM_z = \int n_e^2 dz$—of the emitting material, so we can map out the density profile of the ejecta just by watching the evolution of the radio emission (Bode & Evans 2008). The early time radio can also show unexpected behavior that can be used to constrain other parameters of the nova event.

5.1. *Observations and Reduction*

We obtained sensitive radio observations of V1324 Sco between 2012 June 26 and 2014 December 19 with the Karl G. Jansky Very Large Array (VLA) through programs S4322, 12A-483, 12B-375, 13A-461, 13B-057, and S61420. Over the course of the nova, the VLA was operated in all configurations, and data were obtained in the C (4–8 GHz), Ku (12–18 GHz), and Ka (26.5–40 GHz) bands, resulting in coverage from 4–37 GHz. Observations were acquired with 2 GHz of bandwidth and 8-bit samplers, split between two independently tunable 1-GHz-wide basebands. The details of our observations are given in Table 5. V1324 Sco was unresolved in all observations.

At the lower frequencies (C band), the source J1751-2524 was used as the complex gain calibrator, while J1744-3116 was used for gain calibration at the higher frequencies (Ku and Ka bands). The absolute flux density scale and bandpass were calibrated during each run with either 3C48 or 3C286. Referenced pointing scans were used at Ku and Ka bands to ensure accurate pointing; pointing solutions were obtained on both the flux calibrator and gain calibrator, and the pointing solution from the gain calibrator was subsequently applied to our observations of V1324 Sco. Fast switching was used for high-frequency calibration, with a cycle time of ∼2 minutes. Data reduction was carried out using standard routines in AIPS and CASA. Each receiver band was edited and calibrated independently. The calibrated data were

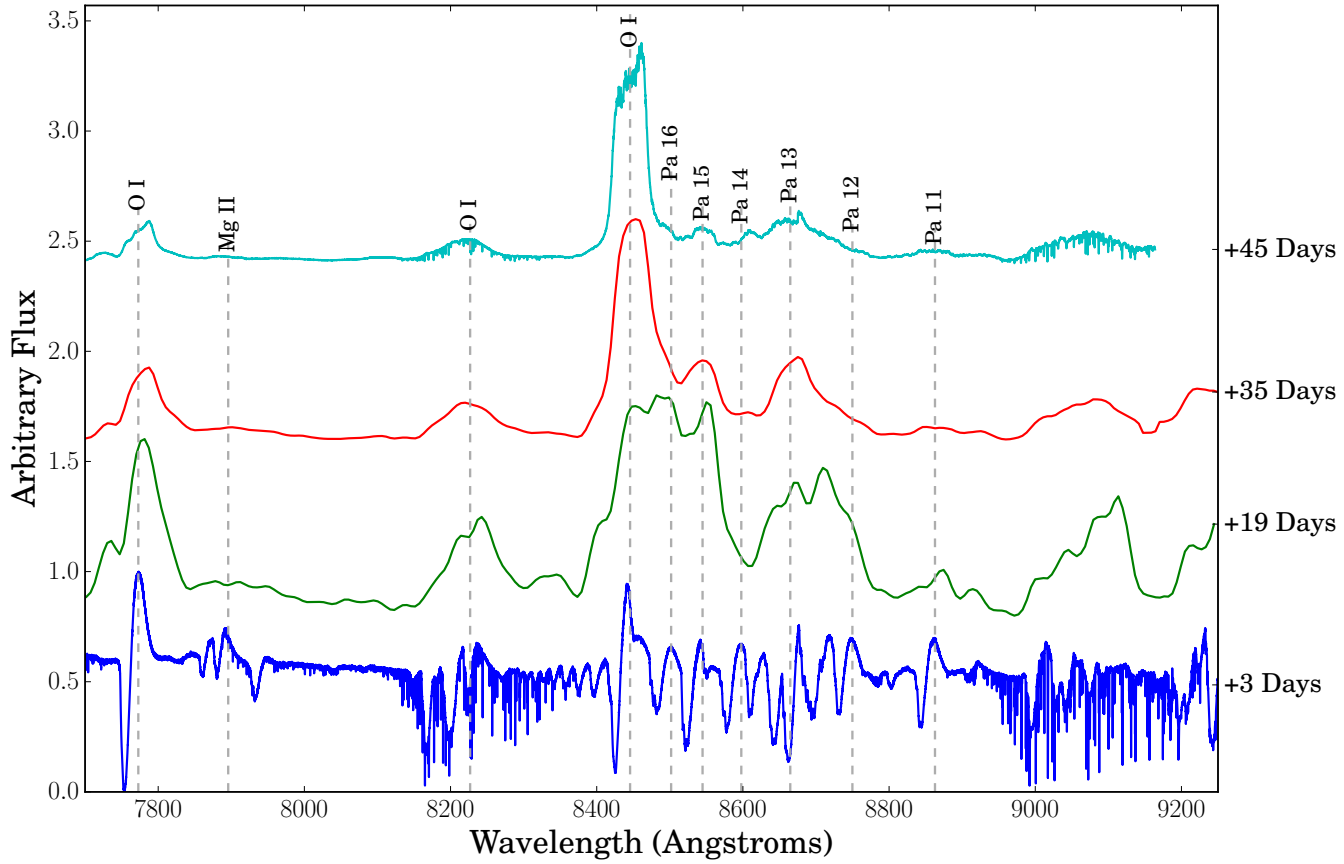

Figure 6. Evolution of the near-infrared (7700 − 9000 Å) spectral region. All wavelengths have been corrected to be in the local standard of rest frame. None of these spectra have been corrected for Telluric features. The UVES spectrum taken on day +3 has prominent contamination from Telluric absorption lines between 8200 Å − 8300 Å and between 8900 Å − 9200 Å.

split into their two basebands and imaged, thereby providing two frequency points.

An observation in A configuration (the most extended VLA configuration) from 2012 Dec 16 suffered severe phase decorrelation at higher frequencies. Despite efforts to self calibrate, we could not reliably recover the source and we therefore do not include these measurements here.

In each image, the flux density of V1324 Sco was measured by fitting a gaussian to the imaged source with the tasks `JMFIT` in AIPS and `gaussfit` in CASA. We record the integrated flux density of the gaussian; in most cases, there was sufficient signal on V1324 Sco to allow the width of the gaussian to vary slightly, but in cases of low signal-to-noise ratio, the width of the gaussian was kept fixed at the dimensions of the synthesized beam. Errors were estimated by the gaussian fitter, and added in quadrature with estimated calibration errors of 5% at lower frequencies (<10 GHz) and 10% at higher frequencies (>10 GHz). All resulting flux densities and uncertainties are presented in Table 5.

5.2. *Timeline of Radio Light Curve*

Here we discuss the different phases of the radio light curve evolution. The radio emission is shown in Figure 8 (radio light curve) and Figure 9 (radio spectra).

5.2.1. *Initial Radio Bump (Days +25 to +136)*

V1324 Sco was detected during the first radio observation (day +25), coincident with the end of the gamma-ray emission and one day before the second X-ray observation. In subsequent radio observations the light curve showed an initial bump, peaking on day +72. The emission after the initial bump—which we refer to as the second bump—was seen 30 to 50 days later (days +102 and +152, respectively; see Figure 8).

The radio spectrum during the initial bump started out flat, with $\alpha = -0.3 \pm 0.7$ on day +25 (where α is defined such that $f_\nu \propto \nu^\alpha$). It then transitioned to $\alpha = 2.0 \pm 0.4$ on day +65, which is consistent with optically thick thermal emission. The spectrum then flattened out again ($\alpha = 0.6 \pm 0.1$ on day +72). Note that the first two epochs were only based on two frequencies (4.5 GHz and 7.8 GHz) while the epoch on day +72 included higher frequency observations (27.5 GHz and 36.5 GHz). As a result, the early time fits should be interpreted with some caution.

A full discussion of the implications for this initial radio bump is given in Section 6.2.2.

5.2.2. *Second Radio Bump (Days +137 to +900)*

After this initial radio bump, a secondary radio bump occurred, starting sometime between September 15 2012 and October 15 2012 (+106 and +136 days after 1 June 2012), starting with high frequencies and progressing to lower frequencies. During this secondary radio bump, V1324 Sco peaked at $\sim$ 6.23 mJy at high frequencies

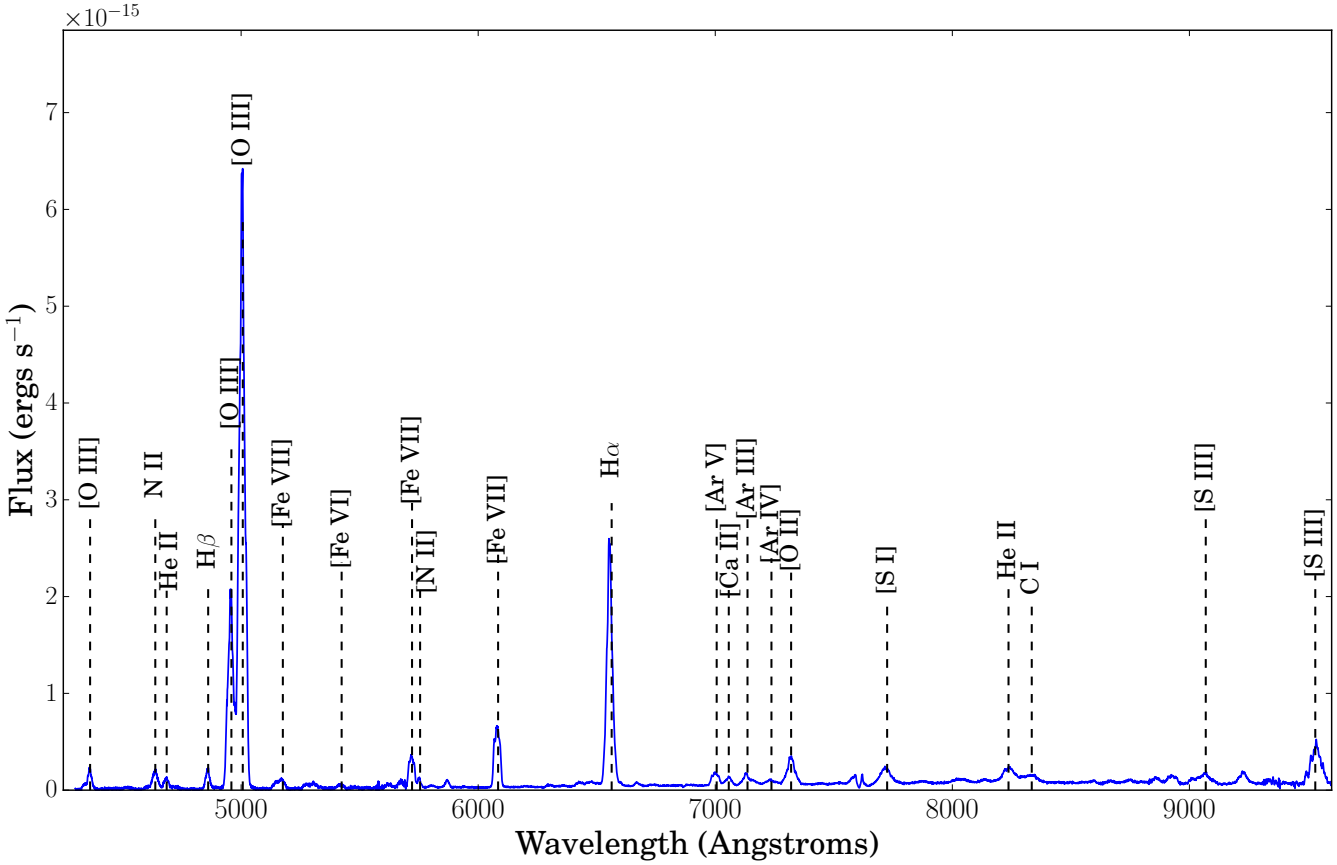

Figure 7. Spectrum for V1324 Sco during the nebular phase taken on day +353.

(36 GHz) between days +218 and +323, and peaked at $\sim$ 1.0 mJy for low frequencies (4.5 GHz) between days +366 and +505. In terms of the evolution of the second radio bump, V1324 Sco was relatively normal compared to the other novae that have been studied in the radio (e.g. Seaquist & Palimaka 1977; Hjellming et al. 1979; Chomiuk et al. 2012; Nelson et al. 2014; Weston et al. 2016). Further analysis of the second radio bump is presented in Section 6.1.2.

6. DISCUSSION

6.1. *V1324 Sco: A Normal Nova*

In this section we make the argument that all of the non-gamma-ray observational signatures of V1324 Sco are normal, in the sense that all of observational features have been seen in previous novae—although never all together in the same novae.

6.1.1. *Optical Regime*

In the optical regime, V1324 Sco is photometrically a *D* (Dusty) class nova (Strope et al. 2010), based on the extraordinary dust event that took place between days +46 to +157. Other *D* class novae include: FH Ser, NQ Vul, and QV Vul. The photometric speed class is consistent with other *D* class novae, all of which are of order tens of days (e.g. FH Ser $t_2 = 49$, days NQ Vul $t_2 = 21$ days, QV Vul $t_2 = 37$ days; see Strope et al. 2010 and references within), with V1324 Sco having a $t_2 \approx 24$ days.

Spectroscopically, V1324 Sco is a Fe II type nova (Williams et al. 1991), due to the prominence of the Fe II spectral features—the second strongest, behind the Balmer features—during optical maximum. The Fe II type classification is common among *D* type novae: FH Ser, NQ Vul, and QV Vul are also Fe II type (see Strope et al. 2010 and references within).

Note that we can also use the spectroscopic observations to determine properties of the ejecta density. Specifically, we use the late-time (nebular) spectroscopy to measure density inhomogeneities (i.e. clumpiness), which we parameterize in terms of the so called filling factor (see Appendix A for the detailed calculations). Such inhomogeneities must be taken into account in order to get a proper mass estimate, and we will incorporate the filling factor in our mass derivation in the next section.

We also use the permitted O I lines at 6300 Å, 7774 Å, and 8446 Å we can constrain the column density (for at least one portion) of the ejecta to be $\geq 10^{25}$ cm^{-2} (see Appendix B for the detailed calculations). As discussed in Section 4, such a high column density can explain the lack of hard X-ray emission.

Such large densities are quite common, as clumpiness is considered to be ubiquitous in novae (see, e.g., Slavin et al. 1995). Taking all of the properties discussed above into account, it is clear that—within the context of the optical regime—V1324 Sco is a normal nova.

6.1.2. *Ejecta Mass as Measured from the Radio Light Curve*

We modeled the secondary radio bump, which we interpret to be thermal emission from the expanding ejecta.

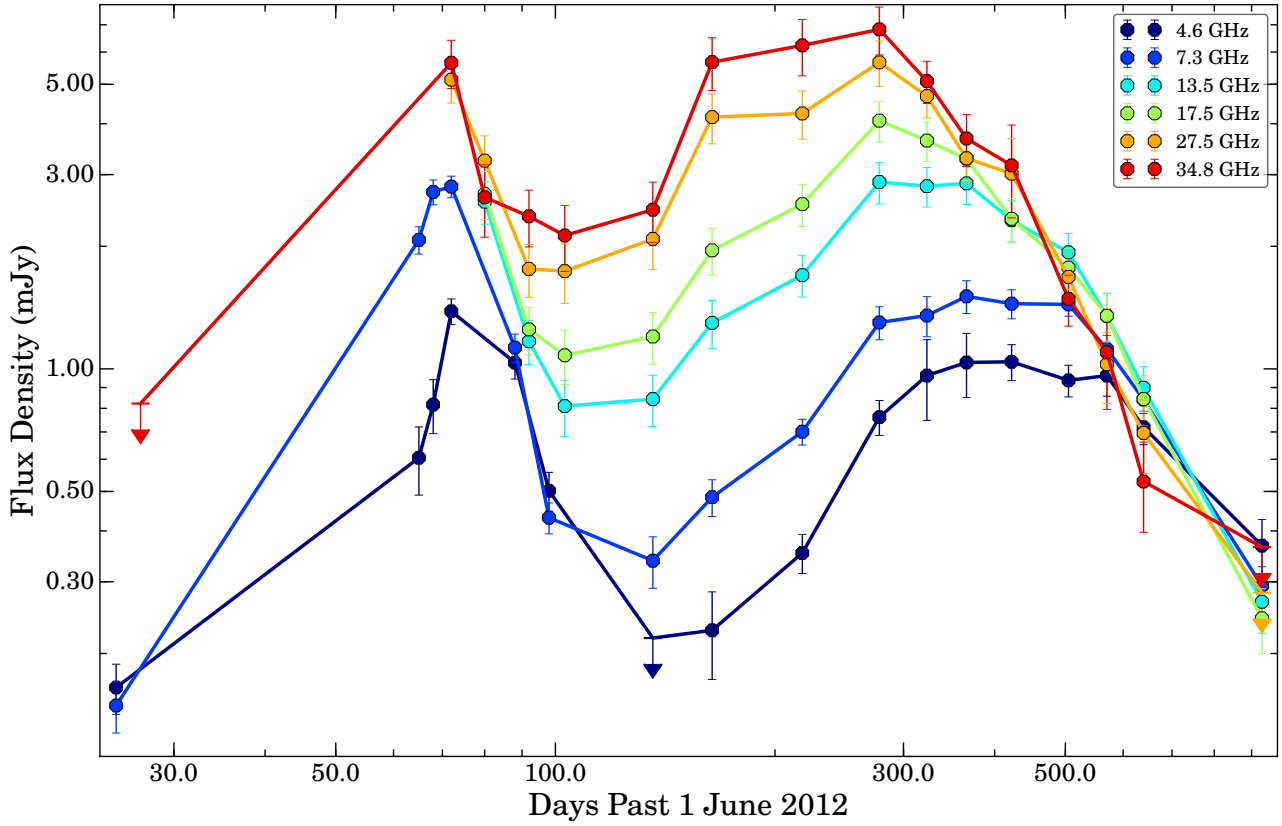

Figure 8. Radio light curve for V1324 Sco, spanning day +22 to day +930 (using June 1 2012 as day 0). Note the initial radio bump seen between day +25 to day +136.

We fit the radio data observed after day +106 (see Figure 8) using the standard model of Hjellming et al. (1979). Specifically, we utilized a homologously expanding Hubble flow model, with an inner and outer radius that is given as a ratio that we refer to as w_{inner}, and an r^{-2} density profile (for more details on this model see Seaquist & Palimaka 1977). The other physical quantities that go into the Hubble flow model (ejecta mass, ejecta velocity, temperature, and distance) are degenerate, and cannot be solved for individually. To circumvent this issue we defined two composite variables that can be determined uniquely. These two variables are defined as

$$\Psi \equiv \frac{T_e v_{\rm ej}^2}{D^2}; \tag{1}$$

$$\xi \equiv T_e^{-3/2} v_{\rm ej}^{-5} \left(\frac{M_{\rm ej} Z}{\bar{\mu}}\right)^2 f_V^{-1}, \tag{2}$$

where T_e is the temperature of the emitting region, $v_{\rm ej}$ is the maximum velocity of the ejecta, D is the distance, $M_{\rm ej}$ is the mass of the ejecta, Z is the average charge of the emitting particles, f_V is the volume filling factor of the ejecta (Discussed further in Appendix A), and $\bar{\mu}$ is the average particle mass. In simple terms we can think of Ψ as setting the flux scale and ξ as setting the time scale for the ejecta to become optically thin, i.e.

$$S_\nu = \Psi t^2 \left[\int_0^{w_{inner}} a(1-e^{-\tau_1(a)})da + \int_{w_{inner}}^1 a(1-e^{-\tau_2(a)})da\right],$$

where S_ν is the observed flux and

$$\tau_1(a) = \frac{\xi t^{-5}}{4\pi[1-w_{inner}]} \int_{\sqrt{w_{inner}-a^2}}^{\sqrt{1-a^2}} \frac{ds}{(a^2+s^2)^2} ds;$$

$$\tau_2(a) = \frac{\xi t^{-5}}{4\pi[1-w_{inner}]} \int_0^{\sqrt{1-a^2}} \frac{ds}{(a^2+s^2)^2} ds,$$

where both integrals have had all of their dimensional parameters put into Ψ and ξ, making them unitless. We also fit the previously mentioned variable w_{inner}—the ratio of the inner and outer radius of the ejecta shell—giving us a total of three variables to fit in our model. A more detailed derivation of this is provided in Finzell et al. (2016, in preparation).

The actual fitting procedure was done using the Markov Chain Monte Carlo program *pymc* (Patil et al. 2010). This procedure was selected as it does not enforce a Gaussian distribution of best fit parameters, allowing us to more accurately characterize the full variance of our results.

Due to the exceptionally large parameter space occupied by our composite variables (many orders of magnitude) our sampling for the MCMC scheme was done in

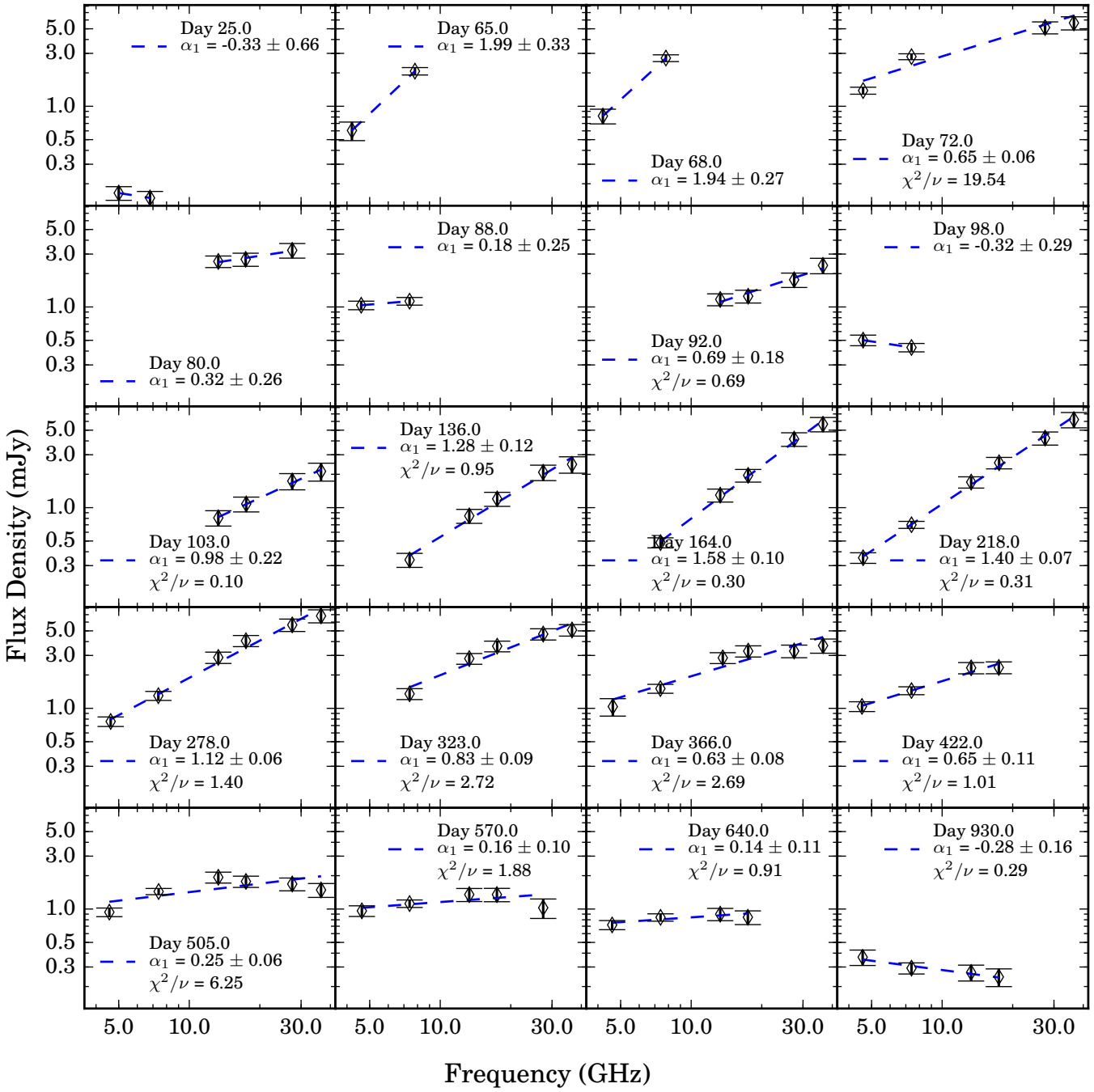

Figure 9. Radio spectra for V1324 Sco. At every epoch with measurements at 3 or more frequencies we fit either a power-law or double power-law to the flux values. The best fit solution was determined by the reduced chi-squared value closest to 1.

log(ξ) and log(Ψ) space, and our results are given as such. Our best set of parameters are $\log(\Psi) = -24.487^{+0.033}_{-0.031}$, $\log(\xi) = 59.763^{+0.03}_{-0.06}$, and $w_{inner} = 0.447^{+0.10}_{-0.079}$.

Figure 10 shows the fit to the second bump using these parameters. The fitting scheme was error weighted, which partially explains why the highest/lowest frequencies are not fit as well. The reduced chi-squared value fit for this model is $\chi^2/\nu = 3.36$. Further, by construction the model has a spectral index of $\alpha = 2.0$ during the rise, as this is the spectral index of an optically thick thermal emission in the Rayleigh-Jeans tail. As can be seen in Figure 9 we never observe a spectral index this high.

We can derive physical parameters for the ejecta—e.g. velocity ($v_{\rm ej}$) and ejected mass ($M_{\rm ej}$)—from ξ and Ψ by using the canonical nova temperature of 10^4 K (Cunningham et al. 2015), the lower bound distance of Finzell et al. (2015) (6.5 kpc), and the filling factor value derived in Section A (also using $T_e = 10^4$ K). The physical quantities derived from this are

$v_{\rm ej}$ =1150 ± 40 km s^{-1}

$M_{\rm ej}$ =2.0 ± 0.4 × 10^{-5} $M_\odot$,

$E_{\rm ej}$ =2.6 ± 0.6 × 10^{44} ergs s^{-1},

where the uncertainty quoted is the 1σ value. The majority of the uncertainty comes from the reddening

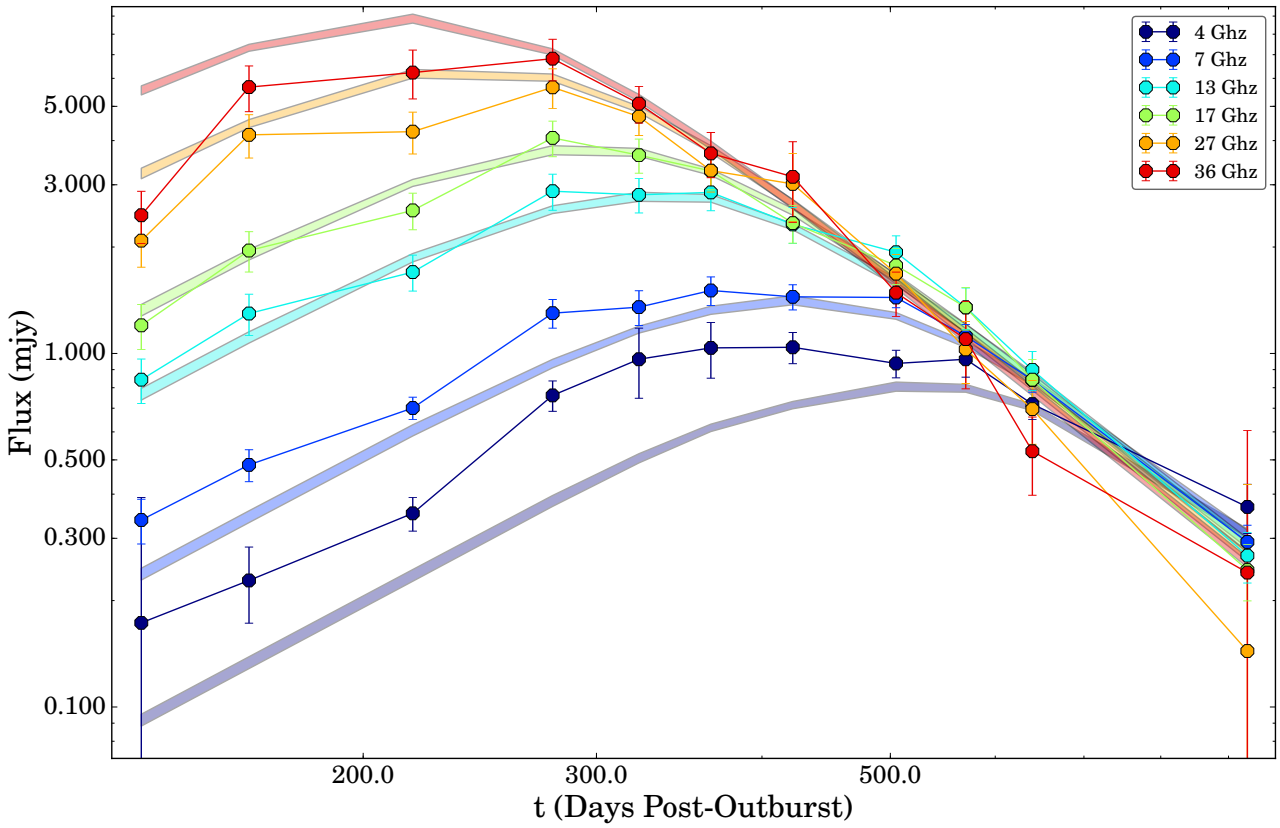

Figure 10. Best fit model to *just* the second bump portion of the radio light curve (see Figure 8 for the entirety of the radio light curve). The best fit parameter values and the resultant physical values can be found in Section 6.1.2. The reduced chi-squared value fit for this model is $\chi^2_{red} = 3.36$. The fitting scheme was error weighted, which (partially) explains the relatively poor fits to the highest and lowest frequencies. There is the further issue of the fact that none of the data have the canonical optically thick spectral index of $\alpha = 2.0$, which the model expects (see Figure 9).

value and a fiducial flux calibration uncertainty.

We have also assumed a fixed temperature and distance in our calculations. Calculating the dependence of $M_{\rm ej}$ on these two variables, we find that

$$
\begin{aligned}
v_{\rm ej} &\propto D\Psi^{1/2}T_e^{-1/2};\\
M_{\rm ej} &\propto \xi^{1/2}T_e^{3/4}v_{\rm ej}^{5/2}f_V^{1/2}\bar{\mu}Z^{-1};\\
f_V &\propto v_{\rm ej}^{-3}T_e^{-1}D^2;\\
\rightarrow M_{\rm ej} &\propto \xi^{1/2}T_e^{3/4}v_{\rm ej}^{5/2}\left[v_{\rm ej}^{-3}T_e^{-1}D^2\right]^{1/2}\bar{\mu}Z^{-1}\\
&= \xi^{1/2}T_e^{1/4}v_{\rm ej}D\bar{\mu}Z^{-1}\\
&= \xi^{1/2}T_e^{1/4}\left[D\Psi^{1/2}T_e^{-1/2}\right]D\bar{\mu}Z^{-1}\\
&= \xi^{1/2}T_e^{-1/4}\Psi^{1/2}D^2\bar{\mu}Z^{-1}.
\end{aligned}
$$

Note that only the power-law contribution to f_V was included, neglecting the *exponential* term. The true dependence on temperature is $M_{\rm ej} \propto T_e^{-1/4}\left[A\exp\left(B/T_e\right)-1\right]^{-1}$, where A and B are constants. As a result, $M_{\rm ej}$ is a very sensitive function of temperature. Given that $M_{\rm ej}$ scales positively with distance (i.e. an increase in distance leads to an increase in $M_{\rm ej}$), and that the distance used was a lower limit, we can think of the $M_{\rm ej}$ derived above as a lower limit.

It should be noted that, during the dust event, we expect some fraction of the nova ejecta to cool, recombine, and become neutral. Since neutral particles won't emit free-free emission—or, at least for atoms with significant dipole moments, they will emit significantly less free-free emission than ionized particles—we don't expect this mass to show up in the radio emission. However, we know from previous studies (see, e.g., Derdzinski et al. 2016 and references within) that the dust mass usually makes up no more than 0.1% of the total ejecta mass, so this discrepancy is negligible.

From the physical properties of the nova event derived above we find that V1324 Sco is very typical (see, e.g. Yaron et al. 2005).

6.1.3. *X-ray Regime*

In the X-ray regime, again, V1324 Sco is normal for a D class nova. Although the three novae we were previously using as examples all went into outburst before there was consistent X-ray monitoring of novae, we know from more recent D class novae that it is the norm—rather than the exception—for dusty novae to go undetected in X-rays. As discussed in Schwarz et al. (2011), only one D class nova has been detected in hard X-rays: V1280 Sco, although this detection was ~ 800 days after the beginning of the nova event. Note: Although not considered a D class nova, Schwarz et al. (2011) makes the case that V2362 Cyg is another dusty nova that has been X-ray detected.

A further two marginally dusty novae have been detected as super-soft-sources (V2467 Cyg and V574 Pup, see Schwarz et al. 2011 and references within). Note that these two sources showed little to no change in their optical light; the presence of dust was only determined due to a modest increase in IR flux. On the other hand, six other dusty novae—including V1324 Sco—were observed but not detected in X-rays (V1324 Sco, V2676 Oph, V2361 Cyg, V1065 Cen, V2615 Oph, and V5579 Sgr; again, see Schwarz et al. 2011).

This lack of X-ray emission in dusty novae could be explained by the cool dense dust forming material absorbing the majority of the X-rays before they can escape. We find that, based on the X-ray observations, V1324 Sco is still a normal nova.

6.1.4. *A Luminous Red Nova?*

A Luminous Red Nova (LRN), observationally, appear brighter and with redder colors than a classical nova (see, e.g., Tylenda et al. 2011). The physical interpretation of these observational characteristics is that a LRN is the result of a merger of a close binary. V1309 Sco is one of the canonical LRNs, and its optical emission is very similar to V1324 Sco. Both have an initial, slow, monotonic rise, both have a flattening of the optical light curve near peak, and both have a significant dust event.

We find, however, that a luminous red nova does not fit with the observations of V1324 Sco. Specifically,

• The most generous estimate of the ejecta mass is still two orders of magnitude smaller than what is expected for LRN events, (Ivanova et al. 2013).

• There is still a detectable period during the power law decline phase of the light curve. This was determined using the MOA data set, which had the best sampling, as well as the highest cadence. The period was measured using the Lomb-Scargle algorithm in the Python scientific library *SciPy*. We limited the data set to $> 5\sigma$ detections.

Some facets of the LRN model, however, could explain features seen in V1324 Sco. For instance, in V1309 Sco, the physical explanation for the light-curve flattening near maximum is that the photosphere does not grow–or grows very slowly–in Eulerian coordinates (and is shrinking in Lagrangian coordinates), due to the fact that the ejecta envelope is cooling, recombining, and becoming optically thin very rapidly. This could also explain the flattening of the optical light curve in V1324 Sco.

Another connection is that the early-slow rise phase of V1309 Sco (see Tylenda et al. 2011) is somewhat similar to that in the rise seen in V1324 Sco. In V1309 Sco the rise was interpreted by Pejcha et al. (2013) as being due to mass loss from L2. Likewise, Chomiuk et al. (2014) interprets the "initial" ejecta phase as being due to a "common-envelope" like ejection, which very well could manifest in its early stage also as L2 mass loss.

6.2. *V1324 Sco: The Most Gamma-Ray Luminous Nova*

Having established in the previous section that V1324 Sco is—in all non gamma-ray observations—a normal nova, we now discuss what about this nova could cause it to have such an extremely high gamma-ray luminosity. There is extremely strong observational evidence for a shock interaction, both from the gamma-rays and from the radio. We discuss here the observational evidence tied to the shock, as well as the physical properties of the nova event—e.g. velocity, density, etc.—that could give rise to differences the in gamma-ray luminosity.

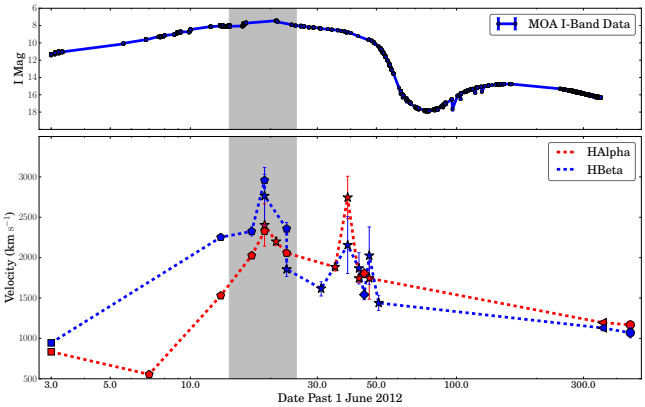

Figure 11. Top Panel: A subset of the I band light curve in Figure 1, given here for reference. Bottom Panel: Evolution of the velocities of both Hα and Hβ. Both velocities are found by taking the Half-Width at Half Maximum HWHM of the spectral feature. The gray shaded region indicates the period of gamma-ray emission (Ackermann et al. 2014). This increase in velocity—coincident with the gamma-ray emission—is interpreted as being a signature of the shock interaction.

6.2.1. *Velocity Variations*

Looking at Figure 3 it is clear that the inferred Balmer line velocities change as a function of time. The spectroscopic velocities for Hα and Hβ are plotted in Figure 11, along with the photometric light curve for comparison purposes. All velocities quoted are half-width at half-maximum (HWHM) measured for each line. A number of the spectra taken by Walter were either blue (3650Å – 5420Å) or red (5620Å – 6940Å); given that Hα and Hβ were were consistently strong in all the spectrum we analyzed, we chose to use these two features for our measurements in order to maximize the number of velocity measurements. The HWHM was measured by fitting a Gaussian profile to the emission lines using the IRAF routine *splot*. The uncertainties were found by adding in quadrature both the uncertainty in the line measurement—found by measuring the line multiple times in *splot*—and the (average) dispersion of the spectrum.

Note that the velocity rises approximately concurrent with the gamma-ray emission (day +14 to +26, marked as a grey shaded region in Figure 11). There are three potential explanations for the observed increase in the Balmer line radial velocity.

• An increase in the ejecta speed. This is what is usually thought to be the case in novae when an increase in Doppler velocity is observed (Kovetz 1998; Schwarz et al. 2001). The best argument against this interpretation is that—along with the increase in velocity—we also see a change in the structure of the spectral profile. Specifically, we see a double horned profile that is characteristic of bipolar ejected material (see Figure 11, between days 31 to 45).

• A recombination wave passing through the outer envelope of the ejecta. This type of model has been proposed

to explain flattening of the optical light curves observed in SNe-II P and Luminous Red Novae, wherein expansion cools the ejecta to the point where hydrogen recombines (see Section 6.1.4 for further details). The now neutral hydrogen can no longer radiate via free-free emission. This process is referred to as a recombination wave, and it would have a significant effect on the structure of the emission lines. We cannot rule out the possibility that a recombination wave is causing the changes in the Balmer emission lines. However, it is unclear if this would necessarily increase the line velocity or just change the shape of the line profile.

• A different, faster, ejecta component—*behind* the previously observed Hα emitting region—slams into the previously observed slower region of material, becoming visible. We find this to be the most likely explanation, as it can explain both the increase in velocity and change in shape of the spectral feature.

It should be noted that this derivation of the velocity is an oversimplification. It is well known that there are multiple velocity components in novae spectra that need to be disentangled (see, e.g., Gill & O'Brien 1999). However, it does serve to put at least some kind of bound on the velocities.

6.2.2. *Early Time Radio Emission*

The initial radio bump—seen in Figure 8 starting on day +25 and going until day $\sim$ 106—is a strong indicator of a shock. The bump was too early to be the thermal emission normally seen in novae. To illustrate the non-thermal nature of the initial radio bump we can use the brightness temperature, which is a the temperature necessary for the observed flux to be purely thermal (assuming some distance and velocity). The equation for brightness temperature is given by

$$T_b(\nu, t) = \frac{S_\nu(t) c^2 D^2}{2\pi k_b \nu^2 (v_{\rm ej} t)^2}, \quad (3)$$

where S_ν is the observed flux, D is the distance, t is the time, and $v_{\rm ej}$ is a fiducial ejecta velocity. We use the brightness temperature as a measure of the deviation from what we would expect from a thermally emitting gas at 10^4 K. Figure 12 shows the maximum brightness temperature as a function of time (using the distance lower limit of 6.5 kpc from Finzell et al. 2015 and a velocity of 1,000 km s^{-1}). Note that two observation epochs (days 80 and 92) were removed due to the lack of low-frequency observations, which usually set the maximum brightness temperature.

This type of initial radio bump has been seen in several other nova, including QU Vul (Taylor et al. 1987, 1988), V1723 Aql (Weston et al. 2016), and V5589 Sgr (Weston et al. 2016) and we are beginning to develop theories to explain such behavior. In Taylor et al. (1987), Metzger et al. (2014), and Weston et al. (2016) it is postulated that the initial radio bumps could be thermal free-free or synchrotron emission—although Weston et al. (2016) come down strongly in favor of the non-thermal model.

To get such high thermal emission at early times, both Taylor et al. (1987) and Metzger et al. (2014) invoke a strong shock as a means for generating hot, free-free emitting gas. Such high temperature gas would also produce significant X-ray emission, which was not observed in V1324 Sco. This can be explained if there is a high column density of material adjacent to the X-ray emitting region (see Section 4).

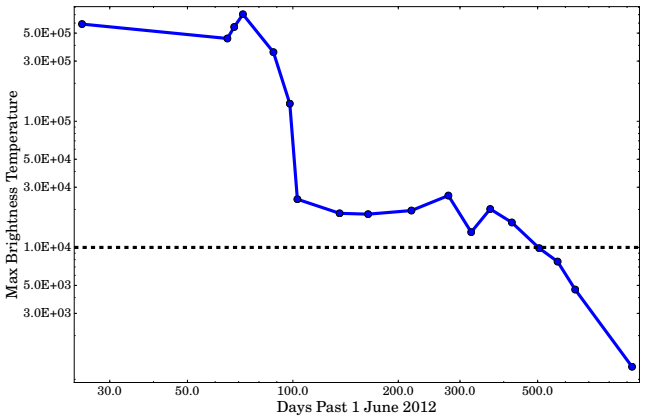

Figure 12. The early time radio bump (day 30 to 50) has maximum brightness temperatures far exceeding that of the canonical 10^4 K thermally emitting ejecta—which can be seen as the dashed black line. The first radio observation, on day +25, occurred while the source was still gamma-ray bright. Note that the observation epochs taken on days 88 and 92 were omitted due to a lack of low-frequency observations.

On the other hand, Taylor et al. (1987) and Vlasov et al. (2016) acknowledge that the emission could be coming from synchrotron emission. In the case of QU Vul, Taylor et al. (1987) invoke the Razin-Tsytovich effect to explain the high spectral-index ($\alpha = 2.42 \pm 0.04$) during the initial radio bump. Vlasov et al. (2016) find that you can also achieve a spectral index > 2.0 when you account for the fact that the expanding ejecta are not isothermal, but have some temperature structure. This is not needed in the case of V1324 Sco, as the spectral index remains at or below 2 throughout the entire initial radio bump.

Vlasov et al. (2016) found that, for low-velocity shocks ($v_{sh} < 1000$ km s^{-1}), line emission dominates the cooling and is very efficient, driving the gas temperature to $T \sim 10^4$ K. This makes it very difficult to achieve the $\sim 10^6$ K gas necessary for the initial radio emission to be explained by thermal emission. The radio data favor a shock velocity $\leq 1,000$ km s^{-1}, as we show in Section 6.1.2. This means that the shock is likely very radiatively efficient, making the thermal emission model for the early radio bump less likely than the non-thermal emission model.

6.2.3. *Physical Parameters of the Shocking Media*

In order to determine what could cause the extreme gamma-ray luminosity, we first determine—in an analytical fashion—the physical quantities that affect the gamma-ray luminosity. We present here a very simplified model of the ejecta that can explain the gamma-ray emission. We can imagine the ejecta as being composed of two parts: a slow initial component and a fast secondary component. When these two components meet, there will be both a forward and reverse shock, and it is these shocks that will power the gamma-ray emission. We further assume that these shocks are radiative, so we expect there to be a layer of cold material between the forward and reverse shocks. Most of this analysis is based on the models of Metzger et al. (2014) and Vlasov et al. (2016).

We assume that the slow component has a density profile given by

$$n_{\rm s}(r) = \left(\frac{\dot{M}_{\rm s}}{4\pi f_\Omega v_{\rm s} r^2 \mu m_p}\right) \exp\left[-\frac{r}{R_{\rm s}}\right], \quad (4)$$

where $\dot{M}_{\rm s}$ is the slow component mass loss rate, μ is the mean molecular weight, f_Ω is the solid angle fraction that is subtended by the slow component, $v_{\rm s}$ is the velocity of the slow component, and $R_{\rm s}$ is the radius of the slow component ($R_{\rm s} = v_{\rm s} t_{\rm s}$, where $t_{\rm s}$ is the time since the slow component was ejected).

Likewise, the fast component has a density profile given by

$$n_{\rm f}(r) \approx \frac{\dot{M}_{\rm f}}{4\pi v_{\rm f} r^2 \mu m_p}, \quad (5)$$

where $\dot{M}_{\rm f}$ is the fast component mass loss rate, $v_{\rm f}$ is the velocity of the fast component.

Assuming that the shocks are radiative, there will be a cold layer of material between the forward and reverse shocks (note that this is also the region where dust will eventually form Derdzinski et al. 2016). We will denote the mass of this shell as $M_{\rm shell}$, which grows in time as

$$\frac{dM_{\rm shell}}{dt} = \dot{M}_{\rm f}\left(\frac{v_{\rm f} - v_{\rm shell}}{v_{\rm f}}\right) + f_\Omega^{-1}\dot{M}_{\rm s}\frac{(v_{\rm shell} - v_s)}{v_s}, \quad (6)$$

while the momentum grows as

$$\frac{d}{dt}\left(M_{\rm shell} v_{\rm shell}\right) = \dot{M}_{\rm f}(v_{\rm f} - v_{\rm shell}) + f_\Omega^{-1}\dot{M}_{\rm s}(v_{\rm shell} - v_{\rm s}). \quad (7)$$

A steady state solution (i.e. $dv_{\rm shell}/dt = 0$) will be reached quickly, wherein the cool shell reaches a final "terminal" velocity. To make this problem more tractable, we assume that $\frac{v_{\rm s}}{v_{\rm f}} << 1$ and $\frac{f_\Omega \dot{M}_{\rm f}}{\dot{M}_{\rm s}} \lesssim 1$. In this limit we find that

$$\frac{v_{\rm shell}}{v_{\rm s}} \approx \left(\frac{\dot{M}_{\rm f} v_{\rm f} f_\Omega}{M_{\rm s} v_{\rm s}}\right)^{1/2}. \quad (8)$$

The power dissipated by the shocks is determined by the number of thermal particles swept up by the shock, which can be expressed as

$$\dot{E}_r = \frac{9}{32} f_\Omega \frac{\dot{M}_{\rm f}}{v_{\rm f}}(v_{\rm f} - v_{\rm shell})^3 \quad (9)$$

$$\dot{E}_f = \frac{9}{32}\frac{\dot{M}_{\rm s}}{v_{\rm s}}(v_{\rm shell} - v_{\rm s})^3. \quad (10)$$

$$(11)$$

Since usually $v_{\rm shell} << v_{\rm f}$, the shock power will be dominated by the reverse shock,

$$L_\gamma \propto \dot{E}_r \approx \frac{9}{32} f_\Omega \dot{M}_{\rm f} v_{\rm f}^2. \quad (12)$$

To determine the amount of time that the gamma-ray emission will persist—hereafter referred to as t_γ—we need to find the amount of time it will take for the shock to cross the initial slow component, i.e. $R_{\rm shell} \approx R_{\rm s} = v_{\rm s} t_{\rm s}$. Rewriting this using our expression for the shock velocity, we find

$$t_\gamma = \frac{R_{\rm s}}{v_{\rm shell}} = \frac{t_{\rm s}\dot{M}_{\rm s} v_{\rm s}}{\dot{M}_f f_\Omega v_{\rm f}}. \quad (13)$$

In the case where $\dot{M}_{\rm f} v_{\rm f} \gg \dot{M}_{\rm s} v_{\rm s}$ (where $t_{\rm s}$ is the amount of time since the slow initial component was ejected). In such a situation t_γ can be simplified to

$$t_\gamma \approx \frac{\dot{M}_{\rm s} v_{\rm s}}{f_\Omega \dot{M}_{\rm f} v_{\rm f}} t_{\rm s} \propto \frac{\dot{M}_{\rm s} v_{\rm s} v_{\rm f}}{L_\gamma} t_{\rm s}. \quad (14)$$

We can see that increasing either $\dot{M}_{\rm f}$ or $v_{\rm f}$ will increase L_γ while decreasing t_γ. This inverse relationship between the gamma-ray luminosity and the duration of the gamma-ray emission has been observed by Cheung et al. (2016).

We posit that it is the fast secondary component that is key in determining the total gamma-ray luminosity, and it is this component that made V1324 Sco the most gamma-ray luminous nova detected to date. It is unclear whether it is the fast component's velocity, mass, or a combination of the two that sets V1324 Sco apart from the other gamma-ray detected novae. This theory can be tested by comparing both the velocity evolution of the ejecta (similar to the analysis of Section 6.2.1) and ejecta mass (similar to the analysis of Section 6.1.2) for multiple gamma-ray detected novae.

7. CONCLUSION

We present here multi-wavelength observations for the most gamma-ray luminous classical nova, V1324 Sco. We demonstrated that this nova was, in all non-gamma-ray observations, a normal nova. Taking a closer look at this normal nova, though, we also see strong evidence for powerful and complex shocks.

Using the optical photometry and spectra we were able to classify V1324 Sco as a *D* (Dusty) photometric class and an Fe II spectral class nova, both of which are common among classical novae. By fitting the evolution of the thermal radio emission we derived a relatively normal ejecta mass of $2.0 \pm 0.4 \times 10^{-5}$ $M_\odot$ and a similarly normal ejecta velocity 1150 ± 40 km s^{-1}.

In spite of this seeming normalcy, we also see strong evidence for shocks, including gamma-ray emission, early time velocity variations coincident with the gamma-ray emission, and early time non-thermal radio emission.

To explain this, we presented a simple model that invokes an ejecta composed of two components: an initial slow component, and a fast secondary component. Using this model, we find that the likely key variables for setting the gamma-ray luminosity are the mass loss rate and velocity of the fast secondary ejecta component. This theory can be put to the test by comparing the velocity variations and ejecta mass of V1324 Sco to other gamma-ray detected novae.

ACKNOWLEDGMENTS

We acknowledge and give thanks to the variable star observations from the AAVSO International Database contributed by observers worldwide and used in this research. This research has made use of the AstroBetter blog and wiki, and was funded in part by the *Fermi*

Guest Observer grant NNX14AQ36G (L Chomiuk). BDM gratefully acknowledges support from NASA Fermi Guest Investigator Program (NNX15AU77G and NNX16AR73G); the National Science Foundation (AST-1615084); and the Research Corporation for Science Advancement Scialog Fellows Program (RCSA 23810). TF thanks B. Broen for helpful comments. The National Radio Astronomy Observatory is a facility of the National Science Foundation operated under cooperative agreement by Associated Universities, Inc.

REFERENCES

Abdo, A. A., Ackermann, M., Ajello, M., et al. 2010, Science, 329, 817
Ackermann, M., Ajello, M., Albert, A., et al. 2014, Science, 345, 554
Aliu, E., Archambault, S., Arlen, T., et al. 2012, ApJ, 754, 77
Bath, G. T., & Shaviv, G. 1976, MNRAS, 175, 305
Berkhuijsen, E. M. 1998, IAU Colloq. 166: The Local Bubble and Beyond, 506, 301
Bhatia, A. K., & Kastner, S. O. 1995, ApJS, 96, 325
Blandford, R. D., & Ostriker, J. P. 1978, ApJ, 221, L29
Blumenthal, G. R., & Gould, R. J. 1970, Reviews of Modern Physics, 42, 237
Bode, M. F., & Evans, A. 2008, Classical Novae, 2nd Edition. Edited by M.F. Bode and A. Evans. Cambridge Astrophysics Series, No. 43, Cambridge: Cambridge University Press, 2008., 43,
Bond, I. A., Abe, F., Dodd, R. J., et al. 2001, MNRAS, 327, 868
Cardelli, J. A., Clayton, G. C., & Mathis, J. S. 1989, apj, 345, 245
Catala, C., & Kunasz, P. B. 1987, A&A, 174, 158
Chesneau, O., Lagadec, E., Otulakowska-Hypka, M., et al. 2012, A&A, 545, A63
Cheung, C. C., Donato, D., Wallace, E., et al. 2010, The Astronomer's Telegram, 2487, 1
Cheung, C. C., Hays, E., Venters, T., Donato, D., & Corbet, R. H. D. 2012, The Astronomer's Telegram, 4224, 1
Cheung, C. C., Glanzman, T., & Hill, A. B. 2012, The Astronomer's Telegram, 4284, 1
Cheung, C. C., Jean, P., Shore, S. N., & Fermi Large Area Telescope Collaboration 2013, The Astronomer's Telegram, 5649,
Cheung, C. C., Jean, P., & Shore, S. N. 2014, The Astronomer's Telegram, 5879,
Cheung, C. C., Jean, P., & Shore, S. N. 2015, The Astronomer's Telegram, 7315, 1
Cheung, C. C., Jean, P., Shore, S. N., et al. 2016, ApJ, 826, 142
Chomiuk, L., Krauss, M. I., Rupen, M. P., et al. 2012, ApJ, 761, 173
Chomiuk, L., Linford, J. D., Yang, J., et al. 2014, Nature, 514, 339
Cunningham, T., Wolf, W. M., & Bildsten, L. 2015, ApJ, 803, 76
Derdzinski, A. M., Metzger, B. D., & Lazzati, D. 2016, arXiv:1610.02401
Drury, L. O., Aharonian, F. A., & Voelk, H. J. 1994, A&A, 287,
Esipov, V. F., Kolotilov, E. A., Komissarova, G. V., et al. 2012, Baltic Astronomy, 21, 47
Finzell, T., Chomiuk, L., Munari, U., & Walter, F. M. 2015, ApJ, 809, 160
Gallagher, J. S., III, & Code, A. D. 1974, ApJ, 189, 303
Gallagher, J. S., & Starrfield, S. 1978, ARA&A, 16, 171
Gallagher, J. S. 1977, AJ, 82, 209
Gehrz, R. D., Jones, T. J., Woodward, C. E., et al. 1992, ApJ, 400, 671
Gill, C. D., & O'Brien, T. J. 1999, MNRAS, 307, 677
Grygar, J., Smoliński, J., & Hutchings, J. B. 1971, PASP, 83, 15
Güver, T., & Oumlzel, F. 2009, MNRAS, 400, 2050
Hachisu, I., & Kato, M. 2016, ApJS, 223, 21
Harrison, T. E., Hamilton, R. T., Tappert, C., Hoffman, D. I., & Campbell, R. K. 2013, AJ, 145, 19
Hays, E., Cheung, T., & Ciprini, S. 2013, The Astronomer's Telegram, 5302, 1
Hillman, Y., Prialnik, D., Kovetz, A., Shara, M. M., & Neill, J. D. 2014, MNRAS, 437, 1962
Hjellming, R. M., Wade, C. M., Vandenberg, N. R., & Newell, R. T. 1979, AJ, 84, 1619
Hornoch, K. 2013, The Astronomer's Telegram, 5621,
Hounsell, R., Bode, M. F., Hick, P. P., et al. 2010, ApJ, 724, 480
Hutchings, J. B. 1972, MNRAS, 158, 177
Ivanova, N., Justham, S., Avendano Nandez, J. L., & Lombardi, J. C. 2013, Science, 339, 433
Kasen, D., Nugent, P., Wang, L., et al. 2003, ApJ, 593, 788
Kastner, S. O., & Bhatia, A. K. 1995, ApJ, 439, 346
Kovetz, A. 1998, ApJ, 495, 401
Kraft, R. P., Burrows, D. N., & Nousek, J. A. 1991, ApJ, 374, 344
Linford, J. D., Ribeiro, V. A. R. M., Chomiuk, L., et al. 2015, ApJ, 805, 136
LSST Science Collaboration, Abell, P. A., Allison, J., et al. 2009, arXiv:0912.0201
Martin, P., & Dubus, G. 2013, A&A, 551, A37
McKee, C. F., & Cowie, L. L. 1975, ApJ, 195, 715
McLaughlin, D. B. 1936, Publications of the American Astronomical Society, 8, 145
Metzger, B. D., Hascoët, R., Vurm, I., et al. 2014, MNRAS, 442, 713
Metzger, B. D., Finzell, T., Vurm, I., et al. 2015, MNRAS, 450, 2739
Metzger, B. D., Caprioli, D., Vurm, I., et al. 2016, MNRAS, 457, 1786
Mróz, P., Udalski, A., Poleski, R., et al. 2015, ApJS, 219, 26
Mukai, K., & Ishida, M. 2001, ApJ, 551, 1024
Mukai, K., Orio, M., & Della Valle, M. 2008, ApJ, 677, 1248
Mukai, K., Nelson, T., Chomiuk, L., Donato, D., & Sokoloski, J. 2012, Baltic Astronomy, 21, 54
Munari, U., Dallaporta, S., Castellani, F., et al. 2013, MNRAS, 435, 771
Munari, U., & Henden, A. 2013, Information Bulletin on Variable Stars, 6087, 1
Nelson, T., Donato, D., Mukai, K., Sokoloski, J., & Chomiuk, L. 2012, ApJ, 748, 43
Nelson, T., Chomiuk, L., Roy, N., et al. 2014, ApJ, 785, 78
Orlando, S., & Drake, J. J. 2012, MNRAS, 419, 2329
Osterbrock, D. E. 1989, Research supported by the University of California, John Simon Guggenheim Memorial Foundation, University of Minnesota, et al. Mill Valley, CA, University Science Books, 1989, 422 p.,
Patil, A., Huard, D., Fonnesbeck., C. 2010, Journal of Statistical Software, 35, 1
Pejcha, O., Antognini, J. M., Shappee, B. J., & Thompson, T. A. 2013, MNRAS, 435, 943
Prialnik, D. 1986, ApJ, 310, 222
Sakon, I., Sako, S., Onaka, T., et al. 2015, arXiv:1507.08801
Schaefer, G. H., Brummelaar, T. T., Gies, D. R., et al. 2014, Nature, 515, 234
Schwarz, G. J., Shore, S. N., Starrfield, S., et al. 2001, MNRAS, 320, 103
Schwarz, G. J., Ness, J.-U., Osborne, J. P., et al. 2011, ApJS, 197, 31
Seaquist, E. R., & Palimaka, J. 1977, ApJ, 217, 781
Sedov, L. I. 1959, Similarity and Dimensional Methods in Mechanics, New York: Academic Press, 1959,
Shore, S. N. 2012, Bulletin of the Astronomical Society of India, 40, 185
Shore, S. N., Wahlgren, G. M., Augusteijn, T., et al. 2012, A&A, 540, A55
Shore, S. N., De Gennaro Aquino, I., Schwarz, G. J., et al. 2013, A&A, 553, A123
Shore, S. N., Mason, E., Schwarz, G. J., et al. 2016, A&A, 590, A123
Skuljan, L., & Bond, I. A. 2012, Publications de l'Observatoire Astronomique de Beograd, 91, 113
Slavin, A. J., O'Brien, T. J., & Dunlop, J. S. 1995, MNRAS, 276, 353
Spitzer, L. 1978, Physical processes in the interstellar medium, by Lyman Spitzer. New York Wiley-Interscience, 1978. 333 p.,
Spruit, H. C., & Taam, R. E. 2001, ApJ, 548, 900
Strope, R. J., Schaefer, B. E., & Henden, A. A. 2010, AJ, 140, 34
Surina, F., Hounsell, R. A., Bode, M. F., et al. 2014, AJ, 147, 107

Taylor, G. 1950, Proceedings of the Royal Society of London Series A, 201, 159
Taylor, A. R., Hjellming, R. M., Seaquist, E. R., & Gehrz, R. D. 1988, Nature, 335, 235
Taylor, A. R., Pottasch, S. R., Seaquist, E. R., & Hollis, J. M. 1987, A&A, 183, 38
Tylenda, R., Hajduk, M., Kamiński, T., et al. 2011, A&A, 528, A114
Vurm, I., & Metzger, B. D. 2016, arXiv:1611.04532
Walter, F. M., Battisti, A., Towers, S. E., Bond, H. E., & Stringfellow, G. S. 2012, PASP, 124, 1057
Wagner, R. M., Dong, S., Bensby, T., et al. 2012, The Astronomer's Telegram, 4157, 1
Wang, L., & Wheeler, J. C. 2008, ARA&A, 46, 433
Weston, J. H. S., Sokoloski, J. L., Metzger, B. D., et al. 2016, MNRAS, 457, 887
Weston, J. H. S., Sokoloski, J. L., Chomiuk, L., et al. 2016, MNRAS, 460, 2687
Williams, R. E., Hamuy, M., Phillips, M. M., et al. 1991, ApJ, 376, 721
Williams, R. 2012, AJ, 144, 98
Vlasov, A., Vurm, I., & Metzger, B. D. 2016, MNRAS, 463, 394
Yaron, O., Prialnik, D., Shara, M. M., & Kovetz, A. 2005, ApJ, 623, 398

APPENDIX

DERIVING FILLING FACTOR

In this Section we derive a means of determining the filling factor, a correction term for the inhomogeneities (clumpiness) of the ejecta. The following derivation of the filling factor is laid out according the following plan: first we find an analytic expression, in terms of measurables, for the filling factor; then, we detail how we measured the variables, the uncertainty for the variables, and how we incorporated the uncertainty into our final calculation.

Derivation

From Berkhuijsen (1998), the filling factor is given by equation 1a,

$$f_V = \frac{\langle n_e^2 \rangle}{n_e^2}, \tag{A1}$$

where $\langle n_e^2 \rangle$ is the average of the density squared. This can be rewritten using equation 4 of the same paper,

$$\langle n_e^2 \rangle = \frac{EM}{L}, \tag{A2}$$

where EM is the emission measure and L is the characteristic length of the emitting material. For our purposes we will assume spherical symmetry of the ejecta and say that the characteristic length is $2v_{\rm ej}t$.

We can determine the emission measure from equation 3-36 in Spitzer (1978),

$$\int I_\nu d\nu = h\nu\alpha_{mn}\left(\frac{n_p}{n_e}\right) \times 2.46 \times 10^{17} E_m. \tag{A3}$$

We modify this to be

$$\int I_\nu d\nu = \frac{\int F_\nu d\nu}{\Omega} \approx \frac{F_\nu \Delta\nu}{\Omega} = \frac{F_\lambda \Delta\lambda}{\Omega}, \tag{A4}$$

where Ω is the solid angle of the source, which we approximate as $(A/D)^2 = \pi(r/D)^2$. r is the ejecta radius, which is just $v_{\rm ej}t$, and D is the distance to the source.

This leads us to the following expression for EM

$$EM = \frac{F_\lambda \Delta\lambda}{h\nu_{H\beta}\alpha_{42}(2.46 \times 10^{17})\Omega} \text{ pc cm}^{-7} \tag{A5}$$

$$= \frac{F_\lambda \Delta\lambda \pi D^2}{h\nu_{H\beta}\alpha_{42}(2.46 \times 10^{17})(v_{\rm ej}t)^2} \text{ pc cm}^{-7}. \tag{A6}$$

Using this expression for EM, we can rewrite equation A2 as

$$\langle n_e^2 \rangle = \frac{F_\lambda \Delta\lambda \pi D^2}{2h\nu_{H\beta}\alpha_{42}(2.46 \times 10^{17})(v_{\rm ej}t)^3} \text{ pc cm}^{-7}. \tag{A7}$$

This expression is in terms of pc cm^{-7}, so we must convert it to cm^{-6}. To do this, we multiply by $\left(\frac{3.086\times10^{18} \text{ cm}}{1 \text{ pc}}\right)$, which gives

$$\langle n_e^2 \rangle = \frac{4\pi^2 F_\lambda \Delta\lambda D^2}{2h\nu_{H\beta}\alpha_{42}(v_{\rm ej}t)^3} \text{ cm}^{-6}. \tag{A8}$$

Finally, we can determine the density by using spectroscopic line ratios. We will use the [O III] line ratio to determine density by using equation 5.4 in Osterbrock (1989)

$$R_{[OIII]} = \frac{j_{\lambda4959} + j_{\lambda5007}}{j_{\lambda4363}} = \frac{7.90\exp(3.29 \times 10^4/T_e)}{1 + 4.5 \times 10^{-4} n_e/T_e^{1/2}}. \tag{A9}$$

This leads to our expression for n_e

$$n_e = \frac{T_e^{1/2}}{4.5 \times 10^{-4}} \left(\frac{7.90 \exp(3.29 \times 10^4 / T_e)}{R_{[OIII]}} - 1 \right) \text{ cm}^{-3}. \tag{A10}$$

Squaring the above expression and combining it with equations A1 and A8, we can now write out our expression for the filling factor.

$$f_V = \left(\frac{2\pi^2 F_\lambda \Delta\lambda D^2}{h\nu_{H\beta}\alpha_{42}(v_{\rm ej}t)^3} \right) \times \left[\frac{T_e^{1/2}}{4.5 \times 10^{-4}} \left(\frac{7.90 \exp(3.29 \times 10^4 / T_e)}{R_{[OIII]}} - 1 \right) \right]^{-2}. \tag{A11}$$

Measured Values and Uncertainty

The unknown values that we need to solve equation A11 are temperature (T_e), distance (D), ejecta velocity ($v_{\rm ej}$), the oxygen line ratio ($R_{[OIII]}$), and the H$_\beta$ flux ($F_\lambda \Delta\lambda$). We use a fiducial value of 10% of the flux as our uncertainty, to account for general calibration uncertainties.

With this value for the uncertainty, we use the iraf tool *splot* to measure an H$_\beta$ flux of $4.19 \pm 0.4 \times 10^{-15}$ ergs cm^{-2} s^{-1}. The line ratio $R_{[OIII]}$ is determined by $j_{\lambda 4959}$, $j_{\lambda 5007}$, and $j_{\lambda 4363}$. We find for these quantities

- $j_{\lambda 4959} = 66.2 \pm 6.6 \times 10^{-15}$ ergs cm^{-2} s^{-1};
- $j_{\lambda 5007} = 218.0 \pm 21.8 \times 10^{-15}$ ergs cm^{-2} s^{-1};
- $j_{\lambda 4363} = 4.8 \pm 0.5 \times 10^{-15}$ ergs cm^{-2} s^{-1}.

As these lines are meant to be a measure of the flux emitted from the source—not the flux measured—we need to make further corrections for interstellar reddening. From Finzell et al. (2015) we know that the reddening is $E(B-V) = 1.16 \pm 0.12$ for V1324 Sco. We use the wavelength specific reddening extinction law of Cardelli et al. (1989) (equations 1 and 3), with an $R_V = 3.1$, to determine the level of extinction. Due to the fact that the denominator of $R_{[OIII]}$ can be very small, the standard deviation of $R_{[OIII]}$ is ill defined. However, once corrected for reddening, we find an $R_{[OIII]}$ value of 29.3 ± 4.4.

For two of the remaining unknown values—T_e and D—we use the same values as section 6.1.2 ($T_e = 10^4$ K, $D = 6.5$ kpc). The remaining value, $v_{\rm ej}$, is derived using the best fit values to the radio data.

Final Value

To determine the final value for f_v we generate distributions of the input variables and plug them into A11, which gives us a distribution of values for f_v. The final value that we quote for f_v is the average of this distribution, and the uncertainty in f_v is the standard deviation of f_v.

We can utilize our distribution of velocities derived in section 6.1.2 to help alleviate some of the uncertainty associated with our measured quantities. From this, and using our canonical nova temperature of 10^4 K and distance of 6.5 kpc, we get a filling factor of

$$f_V = 5.2 \pm 2.2 \times 10^{-2}\ . \tag{A12}$$

The uncertainty is dominated by both the reddening value uncertainty and the fiducial flux calibration uncertainty.

OI DENSITY LIMITS

The strong O I emission at 7774 Å and 8446 Å from the MIKE spectrum—seen in Figure 6—suggests a high density for the emitting material, as the relative strength of the line at 7774 Å compared to 8446 Å is a measure of the rate of collisional deexcitation (Williams 2012). As 8446 Å is a fluorescent line, it should be substantially more dominant than all other O I lines; the only way for 7774 Å to even approach the strength of 8446 Å is if there are very high electron densities, such as at a radiative shock front. The O I line at 6300 Å can also be used as a density diagnostic.

We can use the oxygen line ratios of $j_{\lambda 7774}/j_{\lambda 6300}$ and $j_{\lambda 8446}/j_{\lambda 6300}$ to place constraints on the temperature, density, and ionizing radiation field (Kastner & Bhatia 1995). This technique works best with high spectral resolution measurements, so we use the MIKE spectra taken on day +45. The other high resolution spectra—taken on day +3—had strong, confounding P-Cygni absorption features. After making the necessary reddening corrections (see Section A for more details) we found an average value of $\log(j_{\lambda 7774}/j_{\lambda 6300}) = 0.39 \pm 0.16$ and an average value of $\log(j_{\lambda 8446}/j_{\lambda 6300}) = 1.08 \pm 0.13$.

We can compare this to the work of Kastner & Bhatia (1995) and Bhatia & Kastner (1995), who use a simple model that assumes that the rate of excitation can be simply parameterized in terms of the electron number density (N_e), temperature (T_e), and rate of photoexcitation (R_p). Looking at the tables in Kastner & Bhatia (1995), if we assume a temperature of $T_e = 10,000$ K, these ratios are consistent with density $\log(N_e/[\text{cm}^{-3}]) > 10$. Assuming that the density scales like t^{-3}, we would expect the density to be a factor of ~ 10 times greater during the first X-ray observation than it was on day +45. Combined with the fact that we expect the ejecta to have expanded to $\sim$ a few

$\times 10^{14}$ cm, we derive a column density $\geq 10^{25}$ cm^{-3}. As discussed in Section 4, such a high column density can explain the lack of hard X-ray emission.

We can also calculate the total mass that this density implies. Assuming a velocity of $\sim 1,000$ km s^{-1}, a mean molecular weight of 2.0×10^{-24} grams/particle, and a uniform density, this density would correspond to a total ejecta mass of $\approx 2 \times 10^{-3} M_{\odot}$; such a high ejecta mass is at odds with the mass derived from the radio light curve (discussed in Section 6.1.2). A plausible resolution to this discrepancy is if the line emitting region is the cooling region behind a radiative shock, where we would expect the density to be substantially higher (Metzger et al. 2014).

Table 5
VLA Observations of V1324 Sco

Julian (245000+)	Date (UT)	$t - t_0$	Config.	4.5 GHz Flux [a, b] (mJy)	7.8 GHz Flux (mJy)	13.3 GHz Flux (mJy)	17.4 GHz Flux (mJy)	27.5 GHz Flux (mJy)	36.5 GHz Flux (mJy)
6104.3	6/26/2012	25.0	B	0.165 ± 0.023	0.149 ± 0.021	–	–	–	–
6106.1	6/28/2012	27.0	B	–	–	–	–	–	<0.822
6144.1	8/5/2012	65.0	B	0.605 ± 0.115	2.074 ± 0.160	–	–	–	–
6147.1	8/8/2012	68.0	B	0.817 ± 0.124	2.720 ± 0.191	–	–	–	–
6151.2	8/12/2012	72.0	B	1.385 ± 0.100	2.803 ± 0.171	–	–	5.133 ± 0.636	5.647 ± 0.766
6159.2	8/20/2012	80.0	B	–	–	2.574 ± 0.307	2.690 ± 0.364	3.246 ± 0.489	2.639 ± 0.533
6167.0	8/28/2012	88.0	B	1.036 ± 0.092	1.128 ± 0.089	–	–	–	–
6171.1	9/1/2012	92.0	B	–	–	1.169 ± 0.144	1.250 ± 0.165	1.760 ± 0.261	2.370 ± 0.377
6177.9	9/7/2012	98.0	BnA	0.502 ± 0.055	0.431 ± 0.038	–	–	–	–
6182.1	9/12/2012	103.0	BnA	–	–	0.810 ± 0.128	1.080 ± 0.165	1.738 ± 0.290	2.126 ± 0.392
6215.0	10/15/2012	136.0	A	<0.218	0.338 ± 0.049	0.843 ± 0.121	1.201 ± 0.174	2.085 ± 0.332	2.460 ± 0.415
6243.8	11/12/2012	164.0	A	0.228 ± 0.055	0.484 ± 0.050	1.297 ± 0.174	1.955 ± 0.256	4.153 ± 0.582	5.667 ± 0.838
6297.6	1/5/2013	218.0	A	0.353 ± 0.039	0.701 ± 0.051	1.699 ± 0.198	2.539 ± 0.301	4.240 ± 0.574	6.230 ± 0.983
6357.5	3/6/2013	278.0	D	0.761 ± 0.075	1.300 ± 0.121	2.877 ± 0.337	4.071 ± 0.469	5.660 ± 0.725	6.821 ± 0.917
6402.3	4/20/2013	323.0	D	0.963 ± 0.216	1.352 ± 0.153	2.810 ± 0.313	3.637 ± 0.403	4.677 ± 0.543	5.089 ± 0.605
6445.4	6/2/2013	366.0	DnC	1.037 ± 0.186	1.507 ± 0.139	2.855 ± 0.322	3.283 ± 0.379	3.290 ± 0.429	3.680 ± 0.538
6501.3	7/28/2013	422.0	C	1.041 ± 0.105	1.446 ± 0.118	2.318 ± 0.270	2.337 ± 0.286	3.017 ± 0.659	3.160 ± 0.811
6584.0	10/19/2013	505.0	B	0.937 ± 0.084	1.440 ± 0.093	1.933 ± 0.218	1.773 ± 0.206	1.682 ± 0.222	1.486 ± 0.213
6649.7	12/23/2013	570.0	B	0.963 ± 0.106	1.120 ± 0.087	1.350 ± 0.182	1.350 ± 0.186	1.027 ± 0.205	1.098 ± 0.304
6719.5	3/3/2014	640.0	A	0.719 ± 0.068	0.841 ± 0.064	0.899 ± 0.114	0.843 ± 0.119	0.696 ± 0.143	0.529 ± 0.132
7009.8	12/18/2014	930.0	C	0.368 ± 0.058	0.293 ± 0.034	0.268 ± 0.044	0.244 ± 0.044	<0.282	<0.365

Note. — Taking t_0 to be 1 June 2012

[a] Detections are defined as flux $> 5\sigma$. Non-detections are given as the 5σ upper limits.
[b] If no observations were taken for a given frequency it is denoted by –.